

The $\nabla \cdot \mathbf{B} = 0$ Constraint in Shock-Capturing Magnetohydrodynamics Codes

Gábor Tóth

Department of Atomic Physics, Pázmány Péter sétány 1, 1117 Budapest, Hungary

E-mail: gtoth@hermes.elte.hu

Received June 17, 1999; revised March 23, 2000

Seven schemes to maintain the $\nabla \cdot \mathbf{B} = 0$ constraint numerically are compared. All these algorithms can be combined with shock-capturing Godunov type base schemes. They fall into three categories: the *eight-wave formulation* maintains the constraint to truncation error, the *projection scheme* enforces the constraint in some discretization by projecting the magnetic field, while the five different versions of the *constrained transport/central difference* type schemes conserve $\nabla \cdot \mathbf{B}$ to machine accuracy in some discretization for every grid cell. It is shown that the three constrained transport algorithms, which have been introduced recently, can be recast into pure finite volume schemes, and the staggered representation of the magnetic field is unnecessary. Another two new and simple central difference based algorithms are introduced. The properties of the projection scheme are discussed in some detail, and I prove that it has the same order of accuracy as the base scheme even for discontinuous solutions. I describe a flexible and efficient implementation of the projection scheme using conjugate gradient type iterative methods. Generalizations to resistive MHD, to axial symmetry, and to non-Cartesian grids are given for all schemes. The theoretical discussion is followed by numerical tests, where the robustness, accuracy, and efficiency of the seven schemes and the base scheme can be directly compared. All simulations are done with the Versatile Advection Code, in which several shock-capturing base schemes are implemented. Although the eight-wave formulation usually works correctly, one of the numerical tests demonstrates that its non-conservative nature can occasionally produce incorrect jumps across strong discontinuities. Based on a large number of tests, the projection scheme, one of the new central difference based schemes, and one of the constrained transport schemes are found to be the most accurate and reliable among the examined methods. © 2000 Academic Press

Key Words: numerical approximation; stability and convergence of difference methods; magnetohydrodynamics.

1. INTRODUCTION

There has been a very rapid development towards shock-capturing numerical methods applied to the equations of magnetohydrodynamics (MHD). Without trying to be complete, here is a list of some of the algorithms: the widely used ZEUS code by Stone and Norman [38] is based on a finite difference algorithm with artificial viscosity; DeVore adapted [13] the flux corrected transport (FCT) scheme to the MHD equations; Dai and Woodward [10] generalized the piecewise parabolic method (PPM); Ryu *et al.* [32], Balsara [1, 2], Powell [31], Zachary *et al.* [50], and Tóth [40, 41] implemented total variation diminishing (TVD) type methods using different approximate Riemann solvers; and the simple TVD Lax–Friedrich (TVDLF) method [48] was implemented and tested for the MHD equations by Barmin *et al.* [4] and Tóth and Odstrčil [44].

The modern MHD codes can successfully solve many problems involving all kinds of discontinuities, both in time accurate and steady state applications. Still, there are unresolved arguments about how one should maintain the divergence-free property of the magnetic field in multidimensional MHD calculations. This property is automatically satisfied in one-dimensional simulations where $\partial_y = \partial_z = 0$ and consequently $B_x = \text{const}$, but many discretization methods do not guarantee $\nabla \cdot \mathbf{B} = 0$ in multidimensional simulations.

1.1. Analytic versus Numerical Constraints

There is a big difference between the view of theorists, who would generally insist that $\nabla \cdot \mathbf{B}$ should be exactly zero, and practitioners of numerical MHD, who usually take a more pragmatic approach and are satisfied with $\nabla \cdot \mathbf{B}$ converging to zero as the grid resolution Δx and the time step Δt approach zero. The justification for the latter approach is simple: None of the numerical values agrees with the analytical solution exactly, so why should one insist that a specific combination of them, namely some numerical representation of $\nabla \cdot \mathbf{B}$, should be equal to the analytic value, i.e., zero? Ideally, one would like to have that *particular* representation to be zero, which ensures that no unphysical effects arise. The usual example for such an unphysical effect is acceleration of the plasma parallel to the field lines (even if the unphysical force vanishes with increasing grid resolution, it may be quite a nuisance when an equilibrium flow is to be modeled) [7]. For conservative shock-capturing methods, however, it is impossible to define a particular discrete constraint on the magnetic field that would avoid all unphysical effects. In particular, I prove in Appendix A that a scheme cannot satisfy both the numerical conservation of momentum and the requirement that the discretized acceleration due to the Lorentz force should be exactly perpendicular to the magnetic field in every grid cell. Due to these difficulties, the usual practice is to choose some simple discretization of $\nabla \cdot \mathbf{B}$, but it should be clear that the choice is always somewhat arbitrary.

One way of ensuring a small numerical value for $\nabla \cdot \mathbf{B}$ is to demand that some particular discretization is exactly zero. Another possibility is to set the numerical value of $\nabla \cdot \mathbf{B}$ to zero in the initial and boundary conditions and to trust the scheme to maintain this condition until the end of the simulation to the accuracy of the truncation error. There seems to be no compelling theoretical argument to favor any of these approaches, and only numerical tests can tell which scheme is the most efficient, accurate, and robust for a particular problem.

1.2. Numerical Algorithms

In the context of shock-capturing MHD codes, three approaches became rather popular to handle the $\nabla \cdot \mathbf{B} = 0$ constraint. All three approaches can be regarded as some modification of, or addition to a *base scheme*. The base scheme can be, for example, Harten's TVD [16] or van Leer's TVD-MUSCL [46], or Yee's TVD Lax–Friedrich scheme [48]. It evolves mass, momentum, and energy densities according to the well-established algorithms of computational hydrodynamics. The base scheme is also used in the time integration of the magnetic field, but it is modified in some way to maintain the $\nabla \cdot \mathbf{B} = 0$ constraint. The three approaches differ in how the base scheme is modified regarding the induction equation.

The first approach, in order of simplicity, is the *8-wave formulation* of the MHD equations suggested by Powell [15, 31], which is found to behave better in terms of stability and accuracy than the discretization of the usual conservative form (see Section 2). The 8-wave form can be derived [47] from physical principles if the $\nabla \cdot \mathbf{B} = 0$ Maxwell equation is not used. This approach requires the addition of some source terms (proportional to $\nabla \cdot \mathbf{B}$) and a simple modification of the Riemann solver (if any) of the base scheme. According to the Lax–Wendroff theorem [24], however, only conservative schemes can be expected to get the correct jump conditions and propagation speed for a discontinuous solution. I will examine this issue in Section 3.

The second approach was named *constrained transport* (CT) by Evans and Hawley [14], which simply means a particular finite difference discretization on a staggered grid, which maintains $\nabla \cdot \mathbf{B}$ in a specific discretization. If the initial magnetic field has zero divergence in this discretization, then every time step will maintain that to the accuracy of machine round off error as long as the boundary conditions are compatible with the constraints. DeVore [13] combined the CT approach with one of the first-generation shock-capturing schemes, the flux corrected transport (FCT), to obtain a divergence free solution by FCT. Much later, the now popular Godunov type, Riemann solver based schemes were also combined with the CT discretization by Dai and Woodward [11, 12], by Ryu *et al.* [35], and by Balsara and Spicer [3]. Hereafter, I will refer to these articles as DW, RMJA, and BS, respectively.

In their original form, the algorithms of DW, RMJA, and BS require the introduction of a new staggered magnetic field variable, which is updated by simple finite differences using the interpolated magnetic and velocity fields (DW), the interpolated fluxes (BS), or the interpolated transport fluxes (RMJA) of the base scheme. The scheme designed by Dai and Woodward is a CT type discretization connected to a Godunov type scheme by spatial and temporal interpolations of the magnetic and velocity fields, which I will therefore call *field-interpolated CT scheme* (or field-CT for short), while the schemes of BS and RMJA will be named *flux-interpolated* and *transport-flux-interpolated CT* (or simply flux-CT and transport-flux-CT), respectively. In Subsection 4.4, I will shed a new light on the above CT approaches: there is no need for a staggered magnetic field representation! The schemes can be regarded as modifications of the finite volume style numerical flux function of the base scheme.

I introduce two *new and simple central difference* (CD) approaches, which are analogous to the CT schemes of DW and BS. The CD approaches fit very smoothly into the finite volume type discretization of the base scheme and, for the extremely simple *field-interpolated central difference* (field-CD) scheme, there is no need for spatial interpolation. The three CT and the two CD schemes all belong to the second approach, so I will call them *constrained transport/central difference* (CT/CD) schemes, and they are described in Section 4. The

CT/CD schemes can be generalized to resistive MHD, to axial symmetric calculations, and to arbitrary curvilinear grids.

The *third approach* is the *projection scheme*, which, in the context of MHD, was first suggested by Brackbill and Barnes [7]. The idea is to project the numerical solution \mathbf{B}^* provided by the base scheme onto the subspace of zero divergence solutions by a linear operator, and this projected \mathbf{B} solution is used in the next time step. The projection involves the solution of a Poisson equation. Section 5 will explore the properties of the projection scheme and address many of the incorrect claims widespread about it. In particular, I show that an appropriate implementation of the projection scheme can preserve the conservative properties, the efficiency, and the flexibility (with respect to grid geometry and boundary conditions) of the base scheme. I also prove that the projection scheme is a consistent discretization even for flows containing discontinuities, and it has the same order of accuracy as the base scheme or any CD/CT type discretization. In this paper the projection step is regarded as an integral part of the scheme and not as a “clean up” procedure. I also note that the idea of projection has been successfully used in the numerical modeling of incompressible hydrodynamics, where the $\nabla \cdot \mathbf{v} = 0$ constraint should be fulfilled. There the projection scheme [5, 9] is applied for calculating the pressure or a correction to pressure after the advection equation is solved explicitly.

Another way to keep $\nabla \cdot \mathbf{B}$ exactly zero is to rewrite the MHD equations in terms of the *vector potential* \mathbf{A} instead of the magnetic field $\mathbf{B} = \nabla \times \mathbf{A}$. A disadvantage of this approach is that the order of spatial derivatives increases by one, which reduces the order of accuracy by one (see [14] for a more in-depth discussion). Replacing the magnetic field by the vector potential requires a completely new base scheme, therefore I will not investigate this approach. As it was noted by Evans and Hawley [14], the divergence free magnetic field evolved by the constrained transport and central difference schemes can always be integrated into a vector potential, thus these schemes can be regarded as if they evolved an “underlying” vector potential.

A recent paper by Peterkin *et al.* [29] discusses a finite volume discretization with a cell centered representation of the magnetic field, and the authors claim that their scheme conserves the divergence of the magnetic field defined for “grid vertices” by their Eqs. (36) and (38). Their proof [29, bottom of p. 159], however, contains an error: the equation $\Delta \Phi_{1,i,j,k} = -\Delta \Phi_{1,i+1,j,k}$ does not follow from the statement that “these flux surfaces share an edge and the flux at this edge is computed just once,” since both $\Delta \Phi_{1,i,j,k}$ and $\Delta \Phi_{1,i+1,j,k}$ are calculated as contour integrals along *four edges*, and there is *only one* coinciding edge, while the other three–three terms are independent. Unfortunately, the proof cannot be saved, and their scheme does not maintain the zero divergence property for any discretization of the divergence of the magnetic field.

Another recent paper by Londrillo and Del Zanna [25] describes a higher than 2nd order constrained transport scheme. In contrast with the CT schemes discussed in this paper, their algorithm uses a high order upwinded reconstruction of the staggered representation of the magnetic field for all the equations (and not just for the induction equation). This approach is clearly more consistent than the above described field- and flux-interpolated CT schemes, but their elaborate algorithm cannot be regarded as a simple modification of a base scheme. Although the test results shown for this new CT scheme are very encouraging, it is not clear whether this should be attributed to the higher order accuracy of the whole scheme, to the more consistent CT discretization, or both.

TABLE I
Basic Properties of Schemes

Name	Base scheme	$\nabla \cdot \mathbf{B} = 0$ constraint	Cost ^a	Description	Reference
8-wave	Any	Truncation error	7%	Section 3	[31, 15]
Field-CT	Any	Conserves (15) and (27)	4%	Subsections 4.2 and 4.4	DW [11, 12]
Flux-CT	Any	Conserves (15) and (27)	5%	Subsections 4.3 and 4.4	BS [3]
Tr-flux-CT	One step TVD	Conserves (15) and (27)	6%	Subsections 4.3 and 4.4	RMJA [35]
Field-CD	Any	Conserves (26)	2%	Subsection 4.5	This paper
Flux-CD	Any	Conserves (26)	4%	Subsection 4.5	This paper
Projection	Any	Enforces (26) to be $< \epsilon$	$\approx 20\%$	Section 5	[7]

^a Fraction of CPU time relative to the one-step TVD base scheme is measured for the VAC implementation.

The properties of the seven schemes discussed in this paper are summarized in Table I.

1.3. Fair Comparison

I will compare the performance of the seven schemes and the base scheme on test problems in Section 6. Such a comparison is difficult based on the published numerical tests due to the following reasons: (1) the different numerical approaches to handle the $\nabla \cdot \mathbf{B} = 0$ constraint are combined with different base schemes, which makes the properties of the numerical approach for $\nabla \cdot \mathbf{B} = 0$ and the properties of the underlying scheme indistinguishable; (2) the published numerical tests often hide the bad properties of the scheme, e.g., by using a very high resolution, or by selecting tests that are favourable to the scheme; (3) the accuracy of the solution is difficult to judge from figures.

To make the comparison fair, in this paper a single code, the Versatile Advection Code (VAC [40, 41], see <http://www.phys.uu.nl/~toth/>) will be used, in which all the seven schemes have been implemented and they can be combined with several shock-capturing base schemes. The capabilities of VAC will be briefly described in Subsection 6.1. The numerical test problems will be solved at different resolutions, so that the numerical errors and the convergence properties can be directly and quantitatively compared. It is important to realize that in a real application we are not interested in the numerically obtained value of $\nabla \cdot \mathbf{B}$, since the analytic value is known to be zero. What we are really interested in is the solution in terms of the primitive variables, which are not known analytically. Therefore the accuracy of the schemes will be compared for the physically most relevant quantities, the primitive variables ρ , \mathbf{v} , p , and \mathbf{B} .

I will restrict myself to two-dimensional, time dependent, ideal MHD test problems on Cartesian grids for the following reasons. Three-dimensional tests are extremely time consuming but they are not more challenging for the numerical schemes than two-dimensional problems. A small amount of resistivity typically only makes the simulation easier to do. Resistivity dominated problems, on the other hand, should not probably be solved by the shock-capturing schemes discussed in this paper. Obtaining converged steady state solutions can be rather time consuming as well as difficult, and such problems will be investigated in another paper. Tests on curvilinear grids may be of interest, but these would be difficult to reproduce by many MHD codes designed for Cartesian grids only. The tests presented here, which were all taken from the literature, are easy to reproduce by other practitioners of numerical MHD.

Based on the theoretical arguments and the numerical tests, conclusions will be drawn in Section 7.

2. EQUATIONS AND NOTATION

The conservation form of the resistive MHD equations

$$\frac{\partial \rho}{\partial t} + \nabla \cdot (\rho \mathbf{v}) = 0 \quad (1)$$

$$\frac{\partial \rho \mathbf{v}}{\partial t} + \nabla \cdot (\mathbf{v} \rho \mathbf{v} - \mathbf{B} \mathbf{B}) + \nabla p_{tot} = 0 \quad (2)$$

$$\frac{\partial e}{\partial t} + \nabla \cdot (\mathbf{v} e + \mathbf{v} p_{tot} - \mathbf{B} \mathbf{B} \cdot \mathbf{v} - \mathbf{B} \times \eta \mathbf{J}) = 0 \quad (3)$$

$$\frac{\partial \mathbf{B}}{\partial t} + \nabla \cdot (\mathbf{v} \mathbf{B} - \mathbf{B} \mathbf{v}) + \nabla \times (\eta \mathbf{J}) = 0 \quad (4)$$

express conservation of mass, momentum, energy, and magnetic flux, respectively. The conservative variables are the mass density ρ , the momentum density $\rho \mathbf{v}$, the total energy density e , and the magnetic field \mathbf{B} . The velocity \mathbf{v} , the current density $\mathbf{J} = \nabla \times \mathbf{B}$, and the total pressure $p_{tot} = p + \mathbf{B}^2/2$ together with the thermal pressure

$$p = (\gamma - 1) \left(e - \frac{1}{2} \rho v^2 - \frac{1}{2} \mathbf{B}^2 \right) \quad (5)$$

are derived quantities. The equation parameters are the adiabatic index γ and the resistivity η . Units of \mathbf{B} are chosen such that the vacuum magnetic permeability is unity. In ideal MHD the resistivity is taken to be $\eta = 0$.

For the constrained transport and central difference discretizations, the original form of the induction equation (4) will be used,

$$\frac{\partial \mathbf{B}}{\partial t} + \nabla \times (-\mathbf{v} \times \mathbf{B} + \eta \mathbf{J}) = 0 \quad (6)$$

which directly follows from Faraday's law $\partial \mathbf{B} / \partial t = -\nabla \times \mathbf{E}$ and the general form of Ohm's law $\eta \mathbf{J} = \mathbf{E} + \mathbf{v} \times \mathbf{B}$, where \mathbf{E} is the electric field.

Finally, the subject of this paper is the constraint

$$\nabla \cdot \mathbf{B} = 0. \quad (7)$$

Analytically, this condition is maintained forever if it holds for the initial magnetic field, since taking the divergence of the induction equation (6) results in

$$\frac{\partial \nabla \cdot \mathbf{B}}{\partial t} = \nabla \cdot (-\nabla \times \mathbf{E}) = 0. \quad (8)$$

Numerically, however, the discrete divergence of the discrete curl may not give exactly zero.

The full set of conservative variables ρ , $\rho \mathbf{v}$, e , and \mathbf{B} will be denoted by U . A short notation for the conservative form of the MHD equations (1)–(4) is

$$\frac{\partial U}{\partial t} + \nabla \cdot \mathbf{F} = 0, \quad (9)$$

where \mathbf{F} represents the set of flux vectors for all the variables.

The discretized time levels are indexed by superscripts, and the spatial discretization by subscripts. Cell centers are denoted by integer subscripts (e.g., j, k in 2D), while the locations of cell interfaces are denoted by half integers (e.g., $j + 1/2, k$). Occasionally, time-centered quantities will also be used, e.g., time level $n + 1/2$ corresponds to time $(t^n + t^{n+1})/2$.

The numerical scheme advances the conservative variables from time level n to time level $n + 1$ by the non-linear discrete operator L as

$$U^{n+1} = U^n + L(U^n). \quad (10)$$

The operator corresponding to the *base scheme* will be denoted by L^* which advances U^n to an ‘‘auxiliary’’ solution $U^* = L^*(U^n)$. This auxiliary solution is only used to obtain the final update U^{n+1} .

3. THE 8-WAVE FORMULATION

Already Brackbill and Barnes [7] suggested a non-conservative formulation to reduce the numerical errors associated with the finite numerical divergence of the magnetic field. It is interesting to note that their paper already contains all the source terms, which show up in the non-conservative 8-wave scheme introduced by Powell [15, 31].

Powell found that his approximate Riemann solver based scheme (TVD-MUSCL with Roe-type approximate Riemann solver) often crashed for multidimensional problems due to the accumulation of errors which were associated with high values of $\nabla \cdot \mathbf{B}$. He suggested to start from an alternative form of the MHD equations that can be derived [47] from the hydrodynamic equations, Ohm’s law, the Lorentz force, and the Maxwell equations *except for the $\nabla \cdot \mathbf{B} = 0$ equation*. This *non-conservative form* of the (resistive) MHD equations

$$\frac{\partial \rho \mathbf{v}}{\partial t} + \nabla \cdot (\mathbf{v} \rho \mathbf{v} - \mathbf{B} \mathbf{B}) + \nabla p_{tot} = -(\nabla \cdot \mathbf{B}) \mathbf{B} \quad (11)$$

$$\frac{\partial e}{\partial t} + \nabla \cdot (\mathbf{v} e + \mathbf{v} p_{tot} - \mathbf{B} \mathbf{B} \cdot \mathbf{v} - \mathbf{B} \times \eta \mathbf{J}) = -(\nabla \cdot \mathbf{B}) \mathbf{B} \cdot \mathbf{v} \quad (12)$$

$$\frac{\partial \mathbf{B}}{\partial t} + \nabla \cdot (\mathbf{v} \mathbf{B} - \mathbf{B} \mathbf{v}) + \nabla \times (\eta \mathbf{J}) = -(\nabla \cdot \mathbf{B}) \mathbf{v} \quad (13)$$

differs from the usual conservative form (2)–(4) by the source terms on the right hand sides. All these source terms are proportional to $\nabla \cdot \mathbf{B}$, thus they should always remain zero analytically, but they can become non-zero numerically.

Using the non-conservative form, Powell arrived at a new discretization, the *eight-wave Riemann solver* (the eighth wave is associated with propagation of $\nabla \cdot \mathbf{B}$) together with the non-conservative source terms above, that was found to be numerically robust. It was later found by Tóth and Odstrčil [44] that the non-conservative source terms also improve the accuracy of the flux corrected transport and TVD Lax–Friedrich (TVDLF) schemes that do not involve a Riemann solver. It should be mentioned that Powell introduced the 8-wave Riemann solver for the hyperbolic set of ideal MHD equations, but it is quite trivial to add the parabolic terms $\nabla \cdot (\mathbf{B} \times \eta \mathbf{J})$ and $\nabla \times (\eta \mathbf{J})$ in (12) and (13) as explicit source terms; at least as long as the resistive diffusion time is longer than other dynamical time scales.

The reason behind the improved robustness and accuracy is believed to be the following: using the non-conservative formulation, the small but finite $\nabla \cdot \mathbf{B}$ generated by the

numerical solution does not accumulate at a fixed grid point, rather the “magnetic monopoles” propagate together with the flow. For many problems the 8-wave formulation works well, the errors in $\nabla \cdot \mathbf{B}$ remain small, and the conservation of quantities is satisfactory. In problems containing strong shocks, however, the non-conservative source terms can produce incorrect jump conditions and consequently the scheme can produce incorrect results away from the discontinuity. These errors do not decrease with the grid resolution although the solution seems to converge normally. This phenomenon will be demonstrated in a rotated shock tube problem in Subsection 6.3.

4. CONSTRAINED TRANSPORT AND CENTRAL DIFFERENCE DISCRETIZATIONS

For sake of simplicity, most of the discrete equations will be shown for a two-dimensional uniform Cartesian grid with slab symmetry in the 3rd direction. This includes the possibility of having three magnetic field components (often referred to as 2.5D model), since B_z can be updated by the base scheme without modification as it does not contribute to $\nabla \cdot \mathbf{B} = \partial_x B_x + \partial_y B_y$. Generalization to 3D is quite trivial and many of the 3D formulae can be found in DW and BS. Generalization to axial symmetry and arbitrary curvilinear grids is described in Appendix B.

For sake of clarity, the cell centered representation of the magnetic field will be denoted by capital \mathbf{B} , while the cell interface centered representation by lower case \mathbf{b} in the difference formulae.

4.1. Constrained Transport in Finite Difference Schemes

The *constrained transport* (CT) method by Evans and Hawley [14] applies a staggered grid to maintain the $\nabla \cdot \mathbf{b} = 0$ property for finite difference schemes. The magnetic field components \mathbf{b} are represented on the cell interfaces.

In 2D the b^x component is located at $x_{j+1/2}, y_k$ while the b^y component is at $x_j, y_{k+1/2}$ as shown in Fig. 1. To make the notation similar to DW and RMJA, let us denote the z component of the electric field by $\Omega = E_z = -\mathbf{v} \times \mathbf{B} + \eta \mathbf{J}$. The main idea of the CT algorithm is to place Ω at the cell corners $x_{j+1/2}, y_{k+1/2}$. The induction equation (6) is

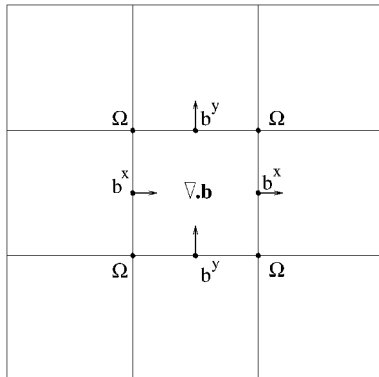


FIG. 1. Staggering in the finite difference constrained transport approach in 2D. The interface centered field components b_x and b_y are updated by finite differencing the electric field Ω located at the cell corners. As a result, $\nabla \cdot \mathbf{b}$ defined in the cell center does not change.

discretized by simple finite differences along the cell edges as

$$\begin{aligned} b_{j+1/2,k}^{x,n+1} &= b_{j+1/2,k}^{x,n} - \Delta t \frac{\Omega_{j+1/2,k+1/2} - \Omega_{j+1/2,k-1/2}}{\Delta y} \\ b_{j,k+1/2}^{y,n+1} &= b_{j,k+1/2}^{y,n} + \Delta t \frac{\Omega_{j+1/2,k+1/2} - \Omega_{j-1/2,k+1/2}}{\Delta x}. \end{aligned} \quad (14)$$

It is easy to show that the numerical divergence of \mathbf{b} defined as

$$(\nabla \cdot \mathbf{b})_{j,k} = \frac{b_{j+1/2,k}^x - b_{j-1/2,k}^x}{\Delta x} + \frac{b_{j,k+1/2}^y - b_{j,k-1/2}^y}{\Delta y} \quad (15)$$

does not change due to perfect cancellation of terms, i.e., if $\nabla \cdot \mathbf{b}^n = 0$ then $\nabla \cdot \mathbf{b}^{n+1} = 0$ to the accuracy of round off errors.

4.2. Field-Interpolated Constrained Transport Scheme

Recently the CT idea was combined with Godunov type schemes by Dai and Woodward. Let us denote the result of the Godunov type base scheme by the superscript $*$. *Spatial and temporal interpolation* is used to obtain the cell corner centered magnetic field

$$\begin{aligned} \bar{\mathbf{B}}_{j+1/2,k+1/2}^{n+1/2} &= \frac{1}{8} (\mathbf{B}_{j,k}^n + \mathbf{B}_{j+1,k}^n + \mathbf{B}_{j,k+1}^n + \mathbf{B}_{j+1,k+1}^n \\ &\quad + \mathbf{B}_{j,k}^* + \mathbf{B}_{j+1,k}^* + \mathbf{B}_{j,k+1}^* + \mathbf{B}_{j+1,k+1}^*) \end{aligned} \quad (16)$$

and velocity field $\bar{\mathbf{v}}_{j+1/2,k+1/2}^{n+1/2}$ (using the same interpolation) at time level $n + 1/2$. On a nonuniform grid, bilinear interpolation could be used. I note that one could interpolate the cell centered $\Omega_{j,k}$ itself, instead of interpolating the components of \mathbf{v} and \mathbf{B} separately, and save some operations.

The z component of the electric field is estimated as

$$\Omega_{j+1/2,k+1/2} = -\bar{\mathbf{v}}_{j+1/2,k+1/2}^{n+1/2} \times \bar{\mathbf{B}}_{j+1/2,k+1/2}^{n+1/2} \quad (17)$$

in ideal MHD, and an extra $\eta \bar{\mathbf{J}}$ term could be added for resistive MHD. After Ω is obtained, the \mathbf{b} field centered at the cell interfaces is updated according to (14). The components of the cell centered \mathbf{B}^{n+1} are obtained by interpolating \mathbf{b} as

$$\begin{aligned} B_{j,k}^{x,n+1} &= \frac{b_{j+1/2,k}^{x,n+1} + b_{j-1/2,k}^{x,n+1}}{2} \\ B_{j,k}^{y,n+1} &= \frac{b_{j,k+1/2}^{y,n+1} + b_{j,k-1/2}^{y,n+1}}{2} \end{aligned} \quad (18)$$

and are used in the next time step. The geometry of the full scheme is depicted in Fig. 2.

4.3. Flux- and Transport-Flux-Interpolated Constrained Transport Schemes

Balsara and Spicer combine the CT approach with an arbitrary Godunov type base scheme by interpolating the appropriately signed cell-interface centered *upwind fluxes* $f^{x,*}$ and $f^{y,*}$

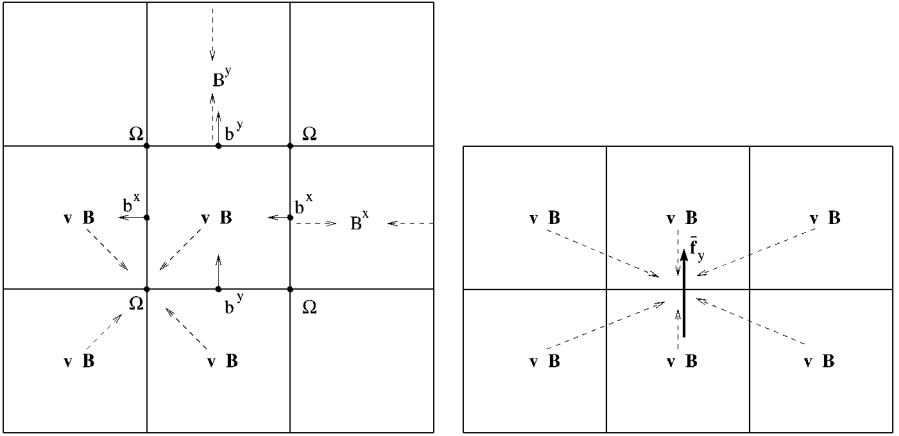


FIG. 2. The staggered (left) and finite volume (right) representations of the field-interpolated CT scheme in 2D. In the staggered approach $\bar{\mathbf{v}}$ and $\bar{\mathbf{B}}$ are interpolated (dashed arrows) from the four neighbouring cells and two time levels. The electric field $\Omega = -\bar{\mathbf{v}} \times \bar{\mathbf{B}}$ is differenced to produce the staggered b_x and b_y , which are interpolated (dashed arrows) to \mathbf{B} . In the finite volume representation the flux \tilde{f}_y is interpolated from 6 cells and 2 time levels. The \tilde{f}_x flux has a similar stencil, but rotated by 90° .

(corresponding to B^y and B^x , respectively) into the electric fields at the cell corners

$$\Omega_{j+1/2,k+1/2} = \frac{1}{4} (-f_{j+1/2,k}^{x,*} - f_{j+1/2,k+1}^{x,*} + f_{j,k+1/2}^{y,*} + f_{j+1,k+1/2}^{y,*}). \quad (19)$$

All four fluxes, with their appropriate signs, are approximations to Ω at the cell interfaces, but they are upwinded according to the base scheme. BS also describes a variant of their scheme, which adjusts the interpolation coefficients in (19) in the vicinity of magnetosonic shocks according to the direction of the local pressure gradient, but they do not find a significant improvement for any of their test cases; therefore I will not use that modification. The electric field $\Omega_{j+1/2,k+1/2}$ can be used to advance the staggered \mathbf{b} field according to the CT approach (14), and \mathbf{B}^{n+1} is obtained by spatial interpolation of \mathbf{b}^{n+1} according to (18). The full flux-CT scheme is depicted in Fig. 3.

Ryu *et al.* (RMJA) suggest yet another way of combining the CT approach with Harten's one step TVD scheme. They define the *transport part* of the upwind fluxes as

$$\begin{aligned} \tilde{f}_{j+1/2,k}^{x,*} &= \frac{(B^y v^x)_{j,k}^n + (B^y v^x)_{j+1,k}^n}{2} + \Phi_{j+1/2,k}^x \\ \tilde{f}_{j,k+1/2}^{y,*} &= \frac{(B^x v^y)_{j,k}^n + (B^x v^y)_{j,k+1}^n}{2} + \Phi_{j,k+1/2}^y, \end{aligned} \quad (20)$$

where the numerical fluxes Φ^x and Φ^y contain the upwind corrections for the TVD property and the Lax–Wendroff type corrections for 2nd order time accuracy, and they are provided by the (approximate) Riemann solver of the base TVD scheme. The partial fluxes $\tilde{f}^{x,*}$ and $\tilde{f}^{y,*}$ can be combined and interpolated into

$$\Omega_{j+1/2,k+1/2} = \frac{1}{2} (-\tilde{f}_{j+1/2,k}^{x,*} - \tilde{f}_{j+1/2,k+1}^{x,*} + \tilde{f}_{j,k+1/2}^{y,*} + \tilde{f}_{j+1,k+1/2}^{y,*}). \quad (21)$$

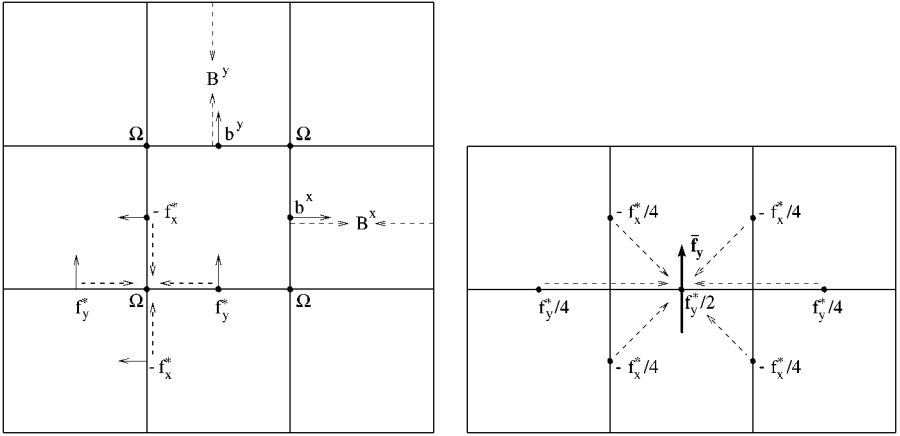


FIG. 3. The staggered (left) and finite volume (right) representations of the flux-interpolated CT scheme in 2D. In the staggered approach the upwind fluxes f_x and f_y are combined (dashed arrows) from the four neighbouring cell interfaces. The resulting electric field estimate Ω is differenced to produce the staggered b_x and b_y , which are interpolated (dashed arrows) to \mathbf{B} . In the finite volume representation the flux \bar{f}_y is combined and interpolated from 6 flux components. The \bar{f}_x flux has a similar stencil, but rotated by 90° .

Note that the denominator is 2 rather than 4 since the transport fluxes contain only a part of the full fluxes. RMJA emphasize a nice property of their transport-flux-CT algorithm: the scheme is identical with the base scheme for one-dimensional problems aligned with one of the coordinate axes. For example, if there is a slab symmetry in the y direction, then $B^x = b^x = \text{const}$ and the upwind correction in the y direction $\Phi_y = 0$, consequently

$$-\Omega_{j+1/2} = \frac{(B^y v^x)_j^n + (B^y v^x)_{j+1}^n}{2} + \Phi_{j+1/2}^x - \frac{(B^x v^y)_j^n + (B^x v^y)_{j+1}^n}{2} \quad (22)$$

which is exactly the one-dimensional *full* upwind flux function f^* of the base scheme for $B_y = b_y$. All the k indices were dropped due to the slab symmetry. This property does not hold for the field-CT and flux-CT approaches.

4.4. Finite Volume Interpretation of CT Schemes

Although DW, BS, and RMJA regard the staggered magnetic field representation \mathbf{b} as the primary variable, in fact it is only used to obtain the cell centered representation \mathbf{B} ; thus one can equally regard \mathbf{B} as the primary variable, which is quite natural in a Godunov-type finite volume scheme. I will show that \mathbf{b} can be eliminated from the CT schemes altogether, which simplifies the implementation (no need for staggered variables), the interpretation in the finite volume sense, and comparison with other schemes.

In fact, the spatial interpolations of the field-CT method (16), (18) can be easily combined into a usual finite-volume-style conservative update

$$B_{j,k}^{x,n+1} = B_{j,k}^{x,n} - \Delta t \frac{\bar{f}_{j,k+1/2}^y - \bar{f}_{j,k-1/2}^y}{\Delta y} \quad (23)$$

$$B_{j,k}^{y,n+1} = B_{j,k}^{y,n} - \Delta t \frac{\bar{f}_{j+1/2,k}^x - \bar{f}_{j-1/2,k}^x}{\Delta x},$$

where the new numerical fluxes are defined as

$$\begin{aligned}\bar{f}_{j+1/2,k}^x &= -\frac{(\bar{\mathbf{v}} \times \bar{\mathbf{B}})_{j+1/2,k+1/2}^{n+1/2} + (\bar{\mathbf{v}} \times \bar{\mathbf{B}})_{j+1/2,k-1/2}^{n+1/2}}{2} \\ \bar{f}_{j,k+1/2}^y &= +\frac{(\bar{\mathbf{v}} \times \bar{\mathbf{B}})_{j+1/2,k+1/2}^{n+1/2} + (\bar{\mathbf{v}} \times \bar{\mathbf{B}})_{j-1/2,k+1/2}^{n+1/2}}{2}\end{aligned}\quad (24)$$

and the rest of the spatial and temporal averaging is hidden in (16). Altogether 6 cells and 2 time levels are averaged out for each flux component. I say *averaging* instead of interpolation, since clearly, the new \bar{f} fluxes require a much wider stencil (see Fig. 2) than the fluxes of the base scheme. The only reason for extending the stencil is to symmetrize the fluxes in such a way that the divergence free property is maintained.

In a similar fashion, the interpolations (18), (19) of the flux-CT scheme can also be combined and the new flux definitions for the components of \mathbf{B} become

$$\begin{aligned}\bar{f}_{j+1/2,k}^x &= \frac{1}{8}(2f_{j+1/2,k}^{x,*} + f_{j+1/2,k+1}^{x,*} + f_{j+1/2,k-1}^{x,*} \\ &\quad - f_{j,k+1/2}^{y,*} - f_{j+1,k+1/2}^{y,*} - f_{j,k-1/2}^{y,*} - f_{j+1,k-1/2}^{y,*}) \\ \bar{f}_{j,k+1/2}^y &= \frac{1}{8}(2f_{j,k+1/2}^{y,*} + f_{j+1,k+1/2}^{y,*} + f_{j-1,k+1/2}^{y,*} \\ &\quad - f_{j+1/2,k}^{x,*} - f_{j+1/2,k+1}^{x,*} - f_{j-1/2,k}^{x,*} - f_{j-1/2,k+1}^{x,*}).\end{aligned}\quad (25)$$

These *averaged* fluxes are used according to (23). For the transport-flux-CT scheme, f^* and the denominator 8 should be replaced by \tilde{f}^* and 4, respectively. Figure 3 shows the total stencils. Note that if the base scheme is dimensionally unsplit, then one can replace the original numerical flux of the base scheme by the above defined \bar{f}^x and \bar{f}^y , and there is no need to calculate a \mathbf{B}^* at all. Again, the required symmetry of the fluxes is achieved via averaging over a wider stencil.

How can one check the divergence-free property of the cell centered \mathbf{B} field if the staggered \mathbf{b} field is eliminated from the algorithm and the implementation? Clearly, the centered difference definition

$$(\nabla \cdot \mathbf{B})_{j,k} = \frac{B_{j+1,k}^x - B_{j-1,k}^x}{2\Delta x} + \frac{B_{j,k+1}^y - B_{j,k-1}^y}{2\Delta y}\quad (26)$$

is not conserved by the CT approach.

It turns out, however, that the following *cell corner centered divergence definition*

$$\begin{aligned}(\nabla \cdot \mathbf{B})_{j+1/2,k+1/2} &= \frac{B_{j+1,k}^x + B_{j+1,k+1}^x - B_{j,k}^x - B_{j,k+1}^x}{2\Delta x} + \frac{B_{j,k+1}^y + B_{j+1,k+1}^y - B_{j,k}^y - B_{j+1,k}^y}{2\Delta y}\end{aligned}\quad (27)$$

vanishes if $\nabla \cdot \mathbf{b} = 0$ for the (j, k) , $(j, k + 1)$, $(j + 1, k)$, and $(j + 1, k + 1)$ cells according to (15), and \mathbf{B} is related to \mathbf{b} according to (18). The above definition (which easily generalizes to nonuniform grids and/or 3D) can be regarded as a contour integral for a diagonally oriented volume shown in Fig. 4. It is also easy to check that if

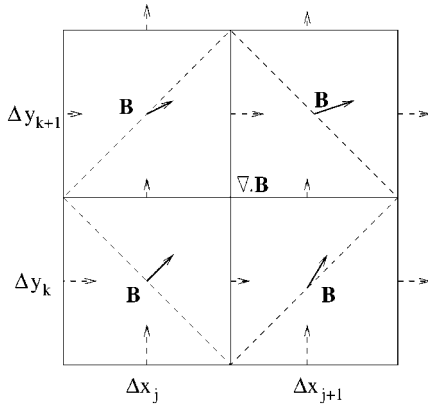


FIG. 4. If the staggered \mathbf{b} field (dashed arrows) satisfies $\nabla \cdot \mathbf{b} = 0$ in all four cells, then $\nabla \cdot \mathbf{B} = 0$ for the diagonally rotated volume (dashed square).

$\nabla \cdot \mathbf{B}^n = 0$ as defined by (27), then applying the fluxes \bar{f} defined by (24) or (25) according to (23) will maintain $\nabla \cdot \mathbf{B}^{n+1} = 0$ in the same sense (27) to the accuracy of round off errors.

In this section, I have recast the field-, flux-, and transport-flux-interpolated CT algorithms into pure finite volume schemes. This shows that these schemes are conservative in the finite volume sense too. In this form, the amount of averaging relative to the base scheme becomes quite apparent. It should be stressed that the above finite volume forms are *identical* with the original staggered schemes in terms of the cell centered variables ρ , ρv , e , and \mathbf{B} . In the next section two new algorithms are introduced, the first of them discards all the spatial averages. The new *central difference* based schemes maintain $\nabla \cdot \mathbf{B} = 0$ in a more natural discretization than (27).

4.5. Field- and Flux-Interpolated Central Difference Schemes

A further step in the direction of simplifying the idea of constrained transport is to use simple *central differencing* (CD) for the induction equation *on the original grid*. To make the scheme second order accurate in time, a *time centered* approximation is taken for the electric field, so, e.g., for ideal MHD

$$\Omega_{j,k} = -(\mathbf{v} \times \mathbf{B})_{j,k}^{n+1/2} = -\frac{(\mathbf{v} \times \mathbf{B})_{j,k}^n + (\mathbf{v} \times \mathbf{B})_{j,k}^{*n}}{2} \tag{28}$$

and the magnetic field is updated as

$$\begin{aligned} B_{j,k}^{x,n+1} &= B_{j,k}^{x,n} - \Delta t \frac{\Omega_{j,k+1} - \Omega_{j,k-1}}{2\Delta y} \\ B_{j,k}^{y,n+1} &= B_{j,k}^{y,n} + \Delta t \frac{\Omega_{j+1,k} - \Omega_{j-1,k}}{2\Delta x}. \end{aligned} \tag{29}$$

It is easy to prove that the central difference definition (26) of $\nabla \cdot \mathbf{B}$ is exactly conserved during the time step, which is more natural than the constraints (15) or (27). The finite volume equivalent of this *field-interpolated* CD approach uses the flux

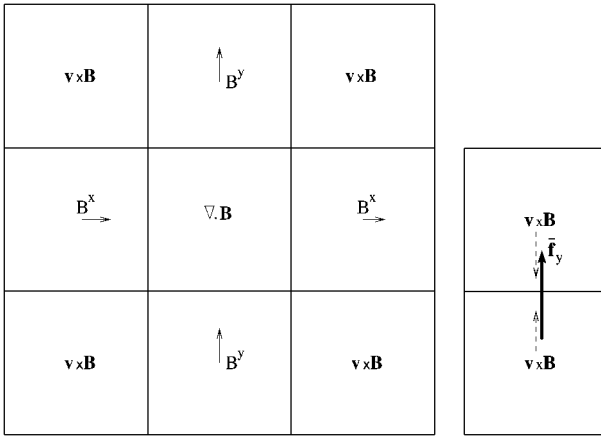


FIG. 5. The field-interpolated central difference (field-CD) approach (left) and its finite volume interpretation (right). The electric field $\Omega = -\mathbf{v} \times \mathbf{B}$ is temporally interpolated between the values obtained from U^n and the auxiliary solution U^* . The magnetic field \mathbf{B} is updated by simple central differencing of Ω . The finite volume flux \bar{f}_y can be obtained from a two-cell stencil, formally. The stencil for \bar{f}_x looks similar, but rotated by 90° .

definitions

$$\begin{aligned}\bar{f}_{j+1/2,k}^x &= -\frac{(\mathbf{v} \times \mathbf{B})_{j,k}^{n+1/2} + (\mathbf{v} \times \mathbf{B})_{j+1,k}^{n+1/2}}{2} \\ \bar{f}_{j,k+1/2}^y &= +\frac{(\mathbf{v} \times \mathbf{B})_{j,k}^{n+1/2} + (\mathbf{v} \times \mathbf{B})_{j,k+1}^{n+1/2}}{2}\end{aligned}\quad (30)$$

in (23) as shown in Fig. 5.

It is also possible to combine the upwind flux components of the base scheme into a cell centered electric field approximation

$$\Omega_{j,k} = \frac{1}{4}(-f_{j-1/2,k}^{x,*} - f_{j+1/2,k}^{x,*} + f_{j,k-1/2}^{y,*} + f_{j,k+1/2}^{y,*}) \quad (31)$$

which can be used in the central difference formula (29). The finite volume flux corresponding to this *flux-interpolated* CD scheme can be easily read from Fig. 6.

It should be emphasized that in the simple central difference formula (29) the electric field Ω is obtained from the shock-capturing base scheme using either temporal interpolation (field-CD scheme) or spatial interpolation (flux-CD scheme). These interpolations provide sufficient coupling between odd and even cells; thus no checker-board like instability arises. The numerical tests also confirm that the CD schemes are stable. Both CD approaches are second order accurate in space for uniform grids and should be “almost” second order accurate for mildly stretched grids. Generalization to arbitrary curvilinear grids is described in Appendix B.

4.6. Boundary and Initial Conditions

The CD and CT approaches maintain $\nabla \cdot \mathbf{B} = 0$ as long as the initial and boundary conditions are compatible with the numerical constraints (26) and (27), respectively. Certain boundary types, e.g., periodic, are easy to implement; others, like inflow, outflow, or a

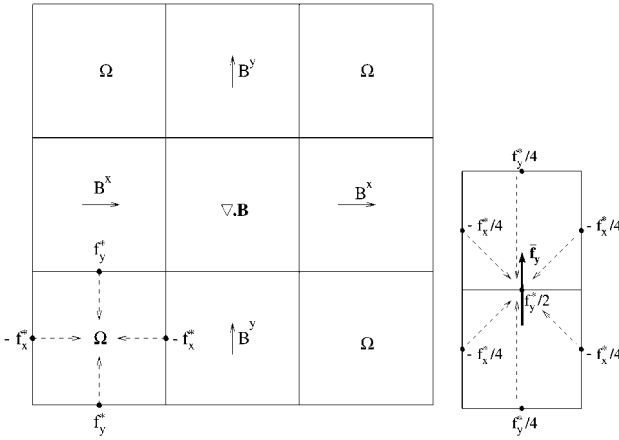


FIG. 6. The flux-interpolated central difference (flux-CD) approach (left) and its finite volume interpretation (right). The cell centered electric field Ω is constructed from the upwind fluxes f^* . The magnetic field \mathbf{B} is updated by simple central differencing of Ω . The finite volume flux \bar{f}_y can be obtained from 6 upwind flux components. The stencil for \bar{f}_x looks similar, but rotated by 90° .

perfectly conducting wall, may require more careful considerations of the discrete form of $\nabla \cdot \mathbf{B} = 0$. In particular, the perfectly conducting wall requires that fluxes are zero across the boundary. For the flux-interpolated CT and CD schemes, the upwind corrections parallel to the boundary can produce a non-zero flux across the boundary if the flux interpolations (19), (21), or (31) are applied carelessly.

The discretized initial conditions given in terms of the magnetic field components do not satisfy the discrete $\nabla \cdot \mathbf{B} = 0$ condition in general. In that case the analytic \mathbf{B} field should be integrated to an analytic vector potential \mathbf{A} , and the discrete $\mathbf{B}_{j,k}$ values should be obtained from finite differencing $\mathbf{A}_{j,k}$ for the CD schemes, or from finite differencing and averaging $\mathbf{A}_{j+1/2,k+1/2}$ for the CT schemes.

5. PROJECTION SCHEME

5.1. Removing the Unphysical Part of the Magnetic Field

The *projection scheme* was proposed by Brackbill and Barnes [7] as a correction to the magnetic field after the time step is completed by some arbitrary numerical scheme. The name comes from the idea that the \mathbf{B}^* field provided by the base scheme in time step $n + 1$ is projected to a divergence-free \mathbf{B}^{n+1} field. It is well known that a vector field can be decomposed unambiguously into the sum of a curl and a gradient

$$\mathbf{B}^* = \nabla \times \mathbf{A} + \nabla \phi, \quad (32)$$

where the curl of the vector potential \mathbf{A} contains the physically meaningful part of \mathbf{B}^* . Taking the divergence of both sides, a Poisson equation

$$\nabla^2 \phi = \nabla \cdot \mathbf{B}^* \quad (33)$$

is obtained, which can be solved for the scalar function ϕ . Then it is easy to correct the magnetic field to

$$\mathbf{B}^{n+1} = \mathbf{B}^* - \nabla \phi. \quad (34)$$

The numerical divergence of \mathbf{B}^{n+1} will be exactly zero if the Laplace operator in (33) is evaluated in two steps as a divergence of the gradient with the same difference operators as used for calculating $\nabla \cdot \mathbf{B}^*$ and $\nabla \phi$ in Eqs. (33) and (34), respectively. If the Laplace operator is evaluated in Fourier space then this requirement translates to Eq. (5.6) in [2]. It follows directly from (34) that the correction does not affect the current density $\mathbf{J} = \nabla \times \mathbf{B}^{n+1} = \nabla \times \mathbf{B}^*$.

5.2. Minimal Correction

Let us solve the following problem: Given the auxiliary solution \mathbf{B}^* with a finite divergence, what is the closest divergence-free \mathbf{B} field? We wish to minimize the function

$$d(\mathbf{B}_1, \mathbf{B}_2, \dots, \mathbf{B}_N) = \frac{1}{2} \|\mathbf{B} - \mathbf{B}^*\|^2 = \frac{1}{2} \sum_{i=1}^N (\mathbf{B}_i - \mathbf{B}_i^*)^2 \quad (35)$$

for the $2N$ unknowns B_i^x, B_i^y with the constraints

$$(\nabla \cdot \mathbf{B})_i = \sum_{j=1}^N D_{i,j}^x B_j^x + D_{i,j}^y B_j^y = 0 \quad (36)$$

for all grid cells indexed by $i = 1 \dots N$. The discrete difference operators D^x and D^y are $N \times N$ matrices, where N is the number of all the grid points. This conditional minimum problem can be solved with the use of the Lagrange multipliers Φ_i , requiring that

$$\frac{\partial [d(\mathbf{B}) + \sum_i \Phi_i (\nabla \cdot \mathbf{B})_i]}{\partial B_j^x} = (B_j^x - B_j^{x,*}) + \sum_i \Phi_i D_{i,j}^x = 0 \quad (37)$$

and similar equations can be obtained for the B_j^y unknowns. The solution is

$$\begin{aligned} B^x &= B^{x,*} - D^{x,T} \Phi \\ B^y &= B^{y,*} - D^{y,T} \Phi, \end{aligned} \quad (38)$$

where the superscripts T indicate transposed operators. To determine the Lagrange multiplier Φ , let us substitute (38) into (36). The final equation for Φ is

$$0 = D^x B^{x,*} + D^y B^{y,*} - (D^x D^{x,T} + D^y D^{y,T}) \Phi. \quad (39)$$

If the discrete operators D^x and D^y are *antisymmetric*, e.g., the central difference operators on a uniform Cartesian grid, then Eqs. (38) and (39) are equivalent with the correction equation (34) and the Poisson equation (33), respectively, and $\phi = -\Phi$.

In other words, on uniform Cartesian grids the projection scheme makes the smallest possible correction to remove the divergence of the magnetic field provided by the base scheme. On nonuniform or non-Cartesian grids the difference operators may not be exactly antisymmetric, still the projected field should be fairly close to the minimal solution. In the continuum limit, the projection provides the solution for the conditional minimum problem.

5.3. Conservation, Consistency and Order of Accuracy

It is quite widely believed that the projection scheme makes an error in the conservation of the total energy and/or in the conservation of the magnetic flux and/or that it cannot be used to obtain discontinuous solutions.

Addressing the first worry is trivial: the total energy e is an independent variable of any numerical scheme that discretizes the MHD equations in a conservation form; thus a change in the magnetic field does not affect the total energy at all. Kinetic energy does not change due to projection either, since momentum and density are not affected. What does change is the magnetic energy, and consequently, the thermal energy, or even more specifically, the temperature. A change of the temperature has no consequences as long as it remains positive, since there is no reason to believe that the temperature associated with U^* was more correct than the one obtained from the projected solution U^{n+1} . Getting a negative temperature can be a problem, of course, but that can occur quite easily independent of the projection scheme too, since the base scheme usually does not guarantee positivity of the temperature either. It could equally occur that the base scheme provides a negative temperature which becomes positive after projection. In certain cases, e.g., when the magnetic energy density is much larger than the thermal energy density, one may prefer to sacrifice the exact conservation of total energy for the sake of robustness. After the projection step the total energy may be modified as

$$e^{n+1} = e^* + \frac{(\mathbf{B}^{n+1})^2 - (\mathbf{B}^*)^2}{2} \quad (40)$$

thus keeping the thermal energy and temperature provided by the base scheme fixed. The same option has been described by BS for their flux-CT algorithm.

Conservation of magnetic flux is a more delicate problem. Of course, magnetic flux is conserved in a global sense, since \mathbf{B}^* is modified by a gradient to obtain \mathbf{B}^{n+1} (34), thus the integrated magnetic flux can only change at the boundaries. What can be more problematic is the conservation of magnetic flux *locally*, especially next to discontinuities, where the correctness of the jump conditions relies on the conservation properties of the scheme and where the divergence of the auxiliary solution \mathbf{B}^* is usually large. In other words, the numerical error in $\nabla \cdot \mathbf{B}^*$ at the discontinuity could be spread all over the computational domain by the projection scheme, and thus the projection scheme would not be consistent or at least the projection would reduce the order of accuracy of the base scheme. Numerical experience shows, however, that the projection scheme does not suffer from this problem: the discontinuities are correctly represented and the numerical error is not increased in the smooth parts of the solution by the projection. The numerical tests in this paper will also support this observation. In the following paragraphs I present a rigorous proof of the consistency of the projection scheme and I also show that its order of accuracy cannot be worse than that of the base scheme or a CT/CD type discretization.

Suppose that we are solving a discontinuous problem. I shall consider a single time step of size Δt starting from an initial condition which is taken to be exact, and I will estimate the error made by the various schemes in one time step. Let me denote the analytic solution after the time step by \mathbf{B}^a . The numerical solution \mathbf{B}^* provided by a consistent and conservative base scheme has to satisfy

$$\|\mathbf{B}^* - \mathbf{B}^a\| < O(\Delta x^k, \Delta t^m), \quad (41)$$

where the norm $\|\cdot\|$ is defined in (35) and the exponents k and m give the actual order of accuracy of the base scheme. For discontinuous problems the order of accuracy is usually lower than it is for smooth problems, but $k > 0$ and $m > 1$ should hold for a sufficiently fine resolution. The solution \mathbf{B}^c provided by any of the CD/CT schemes should also satisfy

$$\|\mathbf{B}^* - \mathbf{B}^c\| < O(\Delta x^{k'}, \Delta t^{m'}) \quad (42)$$

with $k' > 0$, $m' > 1$, and $\nabla \cdot \mathbf{B}^c = 0$ in the appropriate discretisation. As it was proven in Subsection 5.2, the projection scheme changes \mathbf{B}^* to the *closest* divergence-free discrete representation \mathbf{B}^p ; therefore

$$\|\mathbf{B}^p - \mathbf{B}^*\| \leq \|\mathbf{B}^c - \mathbf{B}^*\|. \quad (43)$$

Using simple geometrical inequalities it follows that

$$\begin{aligned} \|\mathbf{B}^p - \mathbf{B}^a\| &\leq \|\mathbf{B}^p - \mathbf{B}^*\| + \|\mathbf{B}^* - \mathbf{B}^a\| \leq \|\mathbf{B}^c - \mathbf{B}^*\| + \|\mathbf{B}^* - \mathbf{B}^a\| \\ &\leq \|\mathbf{B}^c - \mathbf{B}^a\| + 2\|\mathbf{B}^* - \mathbf{B}^a\| < O(\Delta x^{k''}, \Delta t^{m''}), \end{aligned} \quad (44)$$

where the exponents are $k'' = \min(k, k') > 0$ and $m'' = \min(m, m') > 1$; i.e., the projection scheme is a consistent discretization and it has the same order of accuracy as the worse of the base scheme and the CT/CD scheme.

It should be mentioned that the consistency is a necessary but insufficient condition for convergence to the analytic solution at a fixed physical time, because the number of time steps increase with resolution and the growth of the cumulative errors depends on the stability properties of the scheme. Unfortunately, no proof of numerical stability and/or convergence is known for any of the considered base schemes (or for any of the schemes derived from them) when they are applied to a non-linear system of partial differential equations, like the system of MHD equations. Still, it is of practical importance to prove consistency and order of accuracy, otherwise the results of a scheme should not be trusted even if the numerical results seem to suggest stability and convergence for increasing grid resolution.

One can also estimate the change due to a non-zero value of $\nabla \cdot \mathbf{B}^*$ in a single cell. The solution of this problem is the “Green-function” of the discrete Laplace operator. A conservative base scheme, however, will not create a \mathbf{B}^* field containing a single magnetic monopole, since that is not allowed by flux conservation. The error in $\nabla \cdot \mathbf{B}^*$ is the result of an error in \mathbf{B}^* which is due to some flux being too large or too small between two cells. Therefore the “Green function” of the projection scheme is the magnetic field produced by the projection of the field $B_{j,k}^{y,*} = -B_{j+1,k}^{y,*} = 1$ and $\mathbf{B}^* = 0$ everywhere else, which corresponds to a magnetic quadrupole in terms of $\nabla \cdot \mathbf{B}$. The resulting field is depicted in Fig. 7. Clearly, the numerical error causes significant (above 5%) changes only within 4 cells distance from the (j, k) cell. In three dimensions the Green function falls even faster with distance. Since this distance is comparable to the number of cells resolving a typical discontinuity, the projection scheme does not spread the errors significantly.

5.4. Direct versus Iterative Poisson Solvers

The price to pay for the nice properties of the projection scheme is the Poisson problem (33), but that can be solved efficiently with either direct or iterative solvers. *Most direct*

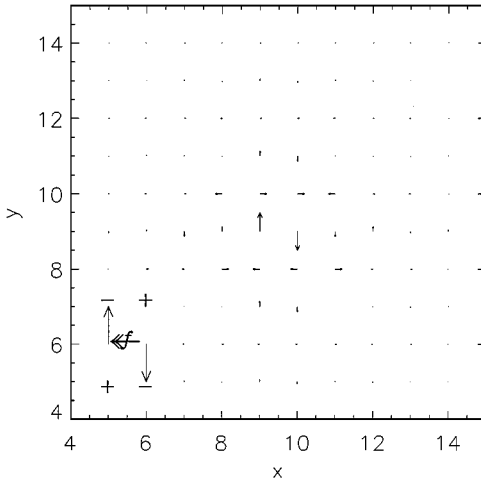


FIG. 7. The “Green function” for the projection scheme. The Green function is the projection of the magnetic field (generated by a single erroneous flux f) shown by the two longest arrows shifted to the bottom left corner. The divergence of this field is a magnetic quadrupole indicated by the + and - signs. The projected divergence-free field is represented by the rest of the arrows centered around the middle of the plot. Note the fast decay of the correction.

Poisson solvers work for relatively special cases, e.g., uniform Cartesian grid with periodic boundary conditions, only, and they require about 20 to 30% of the total CPU time [32, 35]. Another possibility [37] is to calculate the full matrix for the projection operator ($I - \nabla \nabla^{-2} \nabla \cdot$) once and for all and apply it directly in every time step. This direct approach is restricted to moderate grid sizes only, since the memory requirement for the full matrix grows with the square of the number of grid points.

One should realize, however, that unless some discretization of $\nabla \cdot \mathbf{B}$ is particularly optimal for the numerical scheme, the “exact” (to precision of round off errors) solution of the Poisson problem is not necessary. It may well be sufficient to solve the Poisson problem to some accuracy and require that $|\nabla \cdot \mathbf{B}_i^{n+1}| < \epsilon$ where ϵ is a small value relative to the typical $|\nabla \cdot \mathbf{B}^*|$ error generated in one time step. For this particular Poisson problem (33), *iterative solvers* are not just flexible, but also surprisingly efficient. The numerical errors in $\nabla \cdot \mathbf{B}^*$ usually arise as local errors of opposite signs (short wavelength) which are removed by the conjugate gradient type solvers [17, 45] rather efficiently. The very small long wavelength errors do not have to be removed at all, since an approximate solution of the Poisson problem is quite acceptable. For this reason, using a (generally more efficient but much more complicated) multigrid solver for the projection step [50] may not pay off. By applying a few iterations of the conjugate gradient type linear solver, one can reduce the numerically generated divergence of the magnetic field sufficiently. In my experience, the projection scheme with an iterative solver requires about 15% of the total execution time on Cartesian grids (more efficient than direct solvers) and about 30% on general structured grids.

Even on parallel computers, the conjugate gradient type methods are quite efficient and the fraction of the time spent on the projection does not change much by increasing the number of processors [20]. In fact, many of the high-resolution simulations in this paper were done on 16 processors of a Cray T3E parallel computer and the fraction of time spent on the projection remained below 30%.

5.5. Initial and Boundary Conditions

Even if the discretized initial magnetic field has a finite divergence, the projection scheme can eliminate it before the first time step. Therefore the projection scheme is not sensitive to discretization errors in the initial condition. On the other hand, it is important to choose good boundary conditions for ϕ in the Poisson equation (33) so that the corrected magnetic field \mathbf{B}^{n+1} satisfies the boundary conditions for the physical problem. RMJA mentions the restrictions on the boundary conditions as a draw back for the projection scheme. It should be emphasised that *it is not the projection scheme, but their particular Poisson solver* (fast Fourier transform) that restricts the possible boundary conditions to a few simple cases.

Here I briefly describe how the boundary conditions can be implemented when a conjugate gradient (CG) [17], stabilized biconjugate gradient (BiCGSTAB) [45], or similar Krylov subspace type iterative solver is used to solve the Poisson equation. This implementation works successfully in the Versatile Advection Code for a waste number of tests and applications. The iterative schemes require a subroutine which evaluates a matrix vector multiplication: the matrix is the Laplace operator and the vector is an iterate for ϕ . The boundary conditions applied during the evaluation of the discrete Laplace operator will determine the boundary conditions for the solution ϕ and for the magnetic field $\mathbf{B}^{n+1} = \mathbf{B}^* - \nabla\phi$.

The simplest way to implement the boundary conditions is by putting two layers of ghost cells around the physical cells. The unknowns $\phi_{j,k}$ (the description here is for a 2D Cartesian grid, but this can be easily generalized to 3D and/or non-Cartesian grids) belong to the physical cells only, but the two layers are needed, since the Laplace operator is evaluated as the discrete divergence of the discrete gradient, both extending the stencil by one cell in all directions. The values of ϕ in the ghost cells are calculated according to the boundary conditions on the magnetic field. Let me concentrate on the ghost cells next to the $j = 1$ edge of the computational domain and denote the ghost cells by indices 0 and -1 , while the physical cells are indexed from $j = 1$ to N in the x direction.

If \mathbf{B} is *periodic*, ϕ should also be periodic, i.e., $\phi_{-1,k} = \phi_{N-1,k}$ and $\phi_{0,k} = \phi_{N,k}$. For *shifted periodic* boundary conditions $\phi_{-1,k} = \phi_{N-1,k+K}$ and $\phi_{0,k} = \phi_{N,k+K}$, where K is the number of cells by which the periodicity is shifted in the y direction (see Subsection 6.3 for an application). A *fixed* (supersonic inflow or outflow) boundary condition for \mathbf{B} implies that the gradient of ϕ should be zero for the first layer of ghost cells, which can be achieved by setting $\phi_{0,k} = 0$ and $\phi_{-1,k} = \phi_{1,k}$. For a *continuous* (approximation of open) boundary, $\phi_{0,k} = \phi_{-1,k} = 0$ can be used. When the orthogonal component B^x is *antisymmetric* and the tangential component B^y is symmetric (perfectly conducting wall) then the boundary condition on ϕ should be symmetric: $\phi_{-1,k} = \phi_{2,k}$ and $\phi_{0,k} = \phi_{1,k}$. Sometimes the symmetry of the problem demands B^x to be symmetric and B^y antisymmetric at the $x = 0$ boundary, then an antisymmetric condition should be applied on ϕ , i.e., $\phi_{-1,k} = -\phi_{2,k}$ and $\phi_{0,k} = -\phi_{1,k}$.

In summary, the projection scheme can be used efficiently in all geometries for which the Poisson equation can be solved efficiently. Iterative methods provide a very flexible, efficient, and parallelizable algorithm.

6. NUMERICAL TESTS

6.1. Versatile Advection Code

The aim of developing the Versatile Advection Code (VAC) [40, 41] is to provide the astrophysicist and physicist community with a modern, versatile, and user-friendly software,

which can be adapted to the application, and which runs efficiently on work stations, vector and parallel super computers as well.

VAC uses various shock-capturing numerical methods: two versions of flux corrected transport (FCT) schemes [6, 27], the Lax–Wendroff type total variation diminishing (TVD) [16] and the TVD-MUSCL [46] schemes with Roe-type approximate Riemann solvers [33, 34], and the TVD Lax–Friedrichs (TVDLF) method [48]. For the TVD type schemes different slope limiters are available, including the most robust *minmod*, the sharper *monotonized central* (MC, also referred to as Woodward) limiter, and the (overly) sharp *superbee* limiter. For exact specifications of these algorithms, see [44]. In multidimensions, the schemes can be used in a dimensionally split [39] or unsplit manner. Explicit, semi-implicit, or fully implicit time stepping [23, 43] algorithms are available for time integration. The simulations can be done on 1-, 2-, or 3-dimensional structured finite volume grids using the same dimensional independent source code written in the *loop annotation syntax* [42]. In two spatial dimensions both slab and cylindrical symmetry can be assumed in the ignored third dimension. Cartesian and polar grids are handled as special cases for sake of efficiency.

The code is designed to solve conservation laws of the form (9) with possible source terms. The different numerical schemes and equations are implemented in modules and they can be combined arbitrarily. The implemented equation modules are the hydrodynamic and adiabatic hydrodynamic equations, the isothermal or polytropic MHD equations, and the full MHD equations. Source terms for resistivity, viscosity, heat conduction, radiative cooling, and external gravity are readily available; other types of source terms can be defined in user written subroutines.

For MHD applications, the divergence of the magnetic field can be kept zero with the constrained transport or the new central difference approaches (Section 4) or by the projection scheme (Section 5). The Poisson equation (33) is solved by the CG or BiCGSTAB iterative methods. These iterative algorithms work for arbitrary boundary conditions unlike direct solvers based on fast Fourier transforms. Also implemented in VAC are Powell's eight-wave Riemann solver and the corresponding source terms (see Section 3).

Parallel execution of the code is achieved by an automatic translation to high performance Fortran. All explicit schemes, including the iterative Poisson solvers, are fully parallelizable. In this paper VAC will be used as a research tool for computational methods, but it has already been successfully used in many physical applications [18, 19, 21, 22, 26, 30, 36]. The code is available from <http://www.phys.uu.nl/~toth/> via registration.

6.2. Base Scheme and Measurement of Numerical Error

I wish to compare the numerical methods aimed at the $\nabla \cdot \mathbf{B} = 0$ constraint; therefore for any test problem the *base scheme* will be fixed. Since the transport-flux-interpolated CT scheme of RMJA is defined for a one step TVD base scheme only, I chose this method as the base scheme whenever possible. The one step TVD method requires dimensional splitting for numerical stability. Second order accuracy in time is achieved by altering the order of x and y sweeps after every time step the same way as it is done by RMJA and DW. In real applications the time step is varied dynamically based on the Courant–Friedrichs–Lewy (CFL) condition. In principle Δt should only be changed after every second step. If the time step changes in every step, the formal second order temporal accuracy is lost, although the variation of Δt is typically small; thus the error is very small. In any case, in most of the test problems, the time step Δt is set to a fixed value which the final time t_{max} is an integer

multiple of and for which the Courant number is approximately $C = 0.8$ during the whole simulation.

There are a few minor differences between the TVD algorithm used by RMJA and the one used in the test cases below: (1) RMJA use the original flux definition by Harten, while I chose the simpler and equally accurate Roe-type flux (see [44]); (2) I use the monotized central (MC) limiter by default, since it usually gives sharper discontinuities than the minmod limiter and it is simpler than Harten's steepener; (3) no entropy fix was used in these test simulations. Note that these choices are not due to limitations of the Versatile Advection Code but decisions in favour of the better and/or simpler algorithms. VAC actually contains Harten's flux among three others, also Harten's steepener, and four different versions for the entropy fix (including the one used by RMJA). As far as it can be judged from the comparison with several published test results, the base scheme used here is at least as good as the base schemes of RMJA and DW.

For a quantitative comparison of the various schemes handling the $\nabla \cdot \mathbf{B} = 0$ constraint, the numerical error should be calculated and compared. In the absence of an analytic solution, a high resolution numerical solution is used as a basis for comparison. The high resolution solution is *coarsened* to the resolution of the simulations to be compared by averaging out the fine grid values contained in the coarse cells. For example, when the schemes are compared at a 50×50 resolution and the high resolution grid has 400×400 cells, for each coarse cell $8 \times 8 = 64$ high resolution cells are averaged. The averaging corresponds to an integration over the coarse cell, so the coarsened solution is a very accurate numerical solution in the finite volume sense. In principle one should *coarsen the conservative variables* and calculate derived functions of these; however, in certain cases this procedure can lead to non-physical results, e.g., negative temperature. To avoid this possibility, I *coarsen the derived quantities* themselves for the reference solutions used in this paper. As a check, the coarsening was done both ways for a few test problems, and the resulting errors were found to change insignificantly, as expected.

The relative numerical error of variable u obtained on an $N \times M$ grid is defined as

$$\delta u = \frac{\sum_{j=1}^N \sum_{k=1}^M |u_{j,k} - u_{j,k}^{high}|}{\sum_{j=1}^N \sum_{k=1}^M |u_{j,k}^{high}|}, \quad (45)$$

where u^{high} is the coarsened high resolution solution. I will measure the numerical error for the physically most meaningful primitive variables. The averaged error $\bar{\delta}$ is defined as an average of δu for all the (non-zero) primitive variables u . For convergence studies the grid resolution is indicated as a subscript for $\bar{\delta}_N$.

6.3. Rotated One-Dimensional Problems

In all tests of this section, a one-dimensional problem, which can be solved either analytically or very accurately with a 1D simulation, is rotated by an angle α to test the capabilities of the schemes in 2D, where the zero divergence of the magnetic field is not maintained by the base scheme.

When the rotation angle is $\alpha = 0$ (or 90°), the projection, 8-wave, and transport-flux-CT schemes reduce to the base scheme, while the other CD and CT schemes are different from the base scheme even in this slab symmetric case. The $\alpha = \tan^{-1}(\Delta x / \Delta y)$, which is 45° for aspect ratio of unity, case happens to be very special as well: the centered (26) and the staggered (27) discretizations become identical for the diagonal symmetry $\mathbf{B}_{j,k} = \mathbf{B}_{j-1,k+1}$.

Therefore the initial conditions can satisfy $\nabla \cdot \mathbf{B} = 0$ for both discretizations and all the CT and CD schemes will conserve this property. Moreover, due to the symmetry in the x and y fluxes, the flux-CT and flux-CD schemes become identical. Finally, the parallel component of the magnetic field B_{\parallel} (which must be a constant in one-dimensional problems) is also conserved to round off errors by all the CT and CD schemes. This explains why B_{\parallel} and B_{ξ} are almost exactly constant in the plots of RMJA and DW for the rotated shock tube problems. I note that DW incorrectly attribute the minute oscillations in their Fig. 5 in [11] and Fig. 13 in [12] to truncation errors; in fact those oscillation are due to round off errors. For a general angle α , however, the conservation of B_{\parallel} is accurate to truncation errors at best.

6.3.1. Smooth Alfvén waves. This test problem compares the accuracy of the schemes for smooth flow. The *circularly polarized* Alfvén waves are analytic solutions of the MHD equations for arbitrary amplitudes. The test presented in this paper is similar to DW's Alfvén test (Fig. 10 in [12]), but there are significant differences: (1) the Alfvén waves used by DW are *linearly* polarized, therefore the gradient of the magnetic pressure is not zero, which causes a small but finite distortion of the initial sine wave with time; (2) DW sets the fluid velocity $v_{\parallel} = -v_A$ to compensate the Alfvén speed; thus the wave is actually standing relative to the grid. I will use *circularly* polarized Alfvén waves and I will examine both the travelling ($v_{\parallel} = 0$) and standing ($v_{\parallel} + v_A = 0$) wave cases.

It should be mentioned that BS also modeled the propagation of *linearly* polarized oblique Alfvén waves as their third test problem. As I pointed out above, such a travelling wave is *not* an exact solution of the non-linear compressible MHD equations, although the non-linear terms are much smaller than the numerical errors in any of their simulations. The main problem with their test is of a different nature. Balsara and Spicer's third test involves Alfvén waves polarized in the z direction on a two-dimensional x - y domain, while the flux-CT algorithm differs from the base scheme in the B_x and B_y variables only! The latter variables are constants in space and time for this test except for the small non-linear effects. This explains why BS find essentially no difference when the test is done with or without the CT discretization. The tiny differences between their Figs. 5 and 6 should be entirely due to the fact that the non-linear effects slightly perturb B_x and B_y , and these are handled differently by the base scheme and the CT scheme. We shall see that there is a much more pronounced difference between the different discretizations when the Alfvén waves involve the B_x and B_y variables directly.

The circularly polarized Alfvén wave propagates at an angle $\alpha = 30^\circ$ relative to the x axis, and it has a unit wave length in that direction. The computational box is periodic with $0 < x < 1/\cos \alpha$ and $0 < y < 1/\sin \alpha$. The initial conditions are $\rho = 1$, $v_{\parallel} = 0$, $p = 0.1$, $B_{\parallel} = 1$, $v_{\perp} = 0.1 \sin[2\pi(x \cos \alpha + y \sin \alpha)] = B_{\perp}$, and $v_z = 0.1 \cos[2\pi(x \cos \alpha + y \sin \alpha)] = B_z$ with $\gamma = 5/3$ and $\eta = 0$. The $\pi/2$ phase shift between B_z and $B_{\perp} = B_y \cos \alpha - B_x \sin \alpha$ ensures that the magnetic pressure is constant. The Alfvén speed is $|v_A| = B_{\parallel}/\sqrt{\rho} = 1$; thus by time $t = 1$ the flow is expected to return to its initial state. The wave is moving towards $x = y = 0$.

The computational domain is resolved by an $N \times N$ grid; thus the cells have an aspect ratio $\Delta x/\Delta y = \tan \alpha = 1/\sqrt{3}$. For this special choice, the initial condition satisfies $\nabla \cdot \mathbf{B} = 0$ both in the centered (26) and in the staggered (27) discretizations. The simulation is run to a final time $t_{max} = 5$ with a time step $\Delta t = 0.8/N$. The seven schemes and the base scheme are compared for resolutions $N = 8, 16, 32, \text{ and } 64$ in Table II. The errors are averaged for

TABLE II
Convergence of Average Errors for Alfvén Waves

	Travelling waves				Standing waves				
	$\bar{\delta}_8$	$\bar{\delta}_{16}$	$\bar{\delta}_{32}$	$\bar{\delta}_{64}$	$\bar{\delta}_8$	$\bar{\delta}_{16}$	$\bar{\delta}_{32}$	$\bar{\delta}_{64}$	
Projection	0.716	0.135	0.032	0.012	Projection	0.299	0.079	0.031	0.012
Base scheme	0.711	0.133	0.033	0.012	Base scheme	0.321	0.112	0.034	0.013
8-wave	0.713	0.134	0.033	0.012	Flux-CD/CT	0.315	0.122	0.037	0.013
Tr-flux-CT	0.852	0.193	0.044	0.014	Field-CT	0.268	0.102	0.044	0.021
Field-CD	1.016	0.336	0.087	0.025	Field-CD	0.294	0.106	0.044	0.021
Flux-CD/CT	0.971	0.393	0.105	0.029	8-wave	0.351	0.127	0.050	0.024
Field-CT	0.927	0.566	0.163	0.044	Tr-flux-CT	0.549	0.287	0.111	0.046

the v_\perp , v_z , B_\perp , and B_z variables, since the other primitive variables do not take part in the Alfvén wave, and their errors are much smaller. All schemes converge approximately at a second order rate, but there are large differences in the average errors, which is dominated by amplitude and phase errors in B_\perp and v_\perp as shown in Fig. 8.

The simulations were repeated with $v_\parallel = 1$ so that the Alfvén wave is standing relative to the grid. The time step is reduced to $\Delta t = 0.4/N$ to maintain the Courant condition. The results in Table II and Fig. 9 show that the schemes behave rather differently for this setup. The projection scheme and the base scheme are the most accurate for both the travelling and standing wave problems. The transport-flux-CT scheme produces under and overshoots for coarse resolutions.

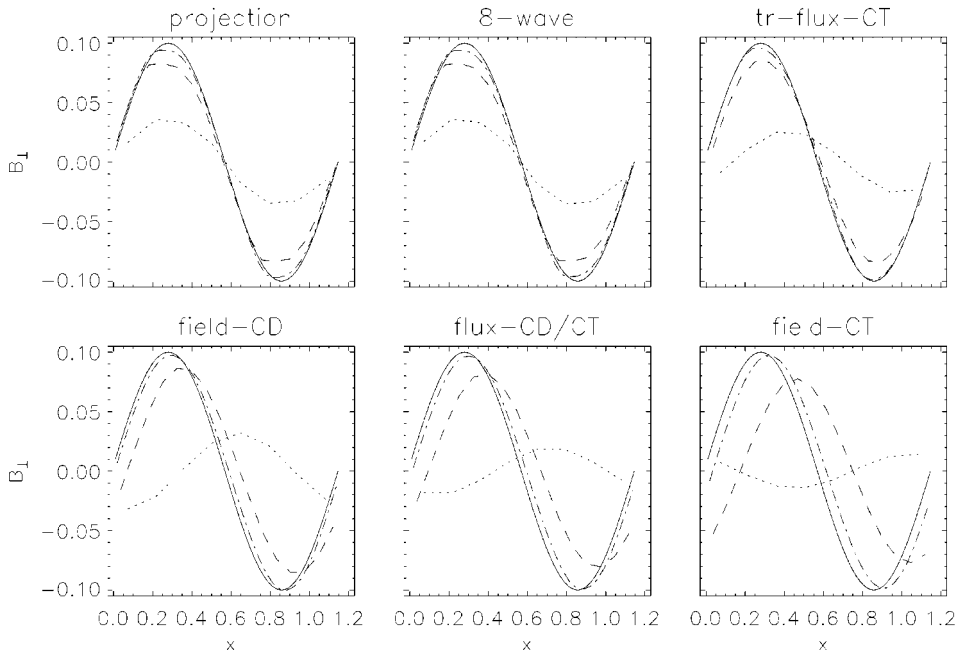


FIG. 8. The orthogonal component $B_\perp = (\sqrt{3}B_y - B_x)/2$ of the magnetic field in the travelling ($v_\parallel = 0$, $v_A = -1$) Alfvén wave problem. The initial condition (full line) is shown for the $N = 64$ resolution. The solutions at time $t = 5$ are shown for the different schemes at resolutions $N = 8$ (dotted), 16 (dashed), and 32 (dot-dash lines).

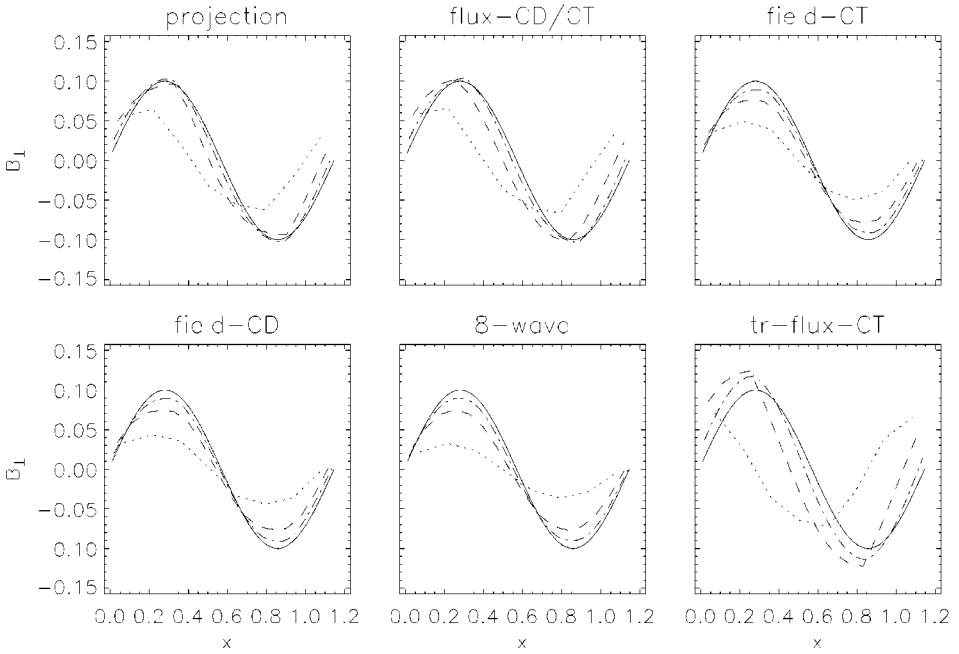


FIG. 9. Conditions the same as Fig. 8 except that the results are shown for the standing ($v_{\parallel} = 1 = -v_A$) Alfvén wave problem.

As a check, I also did the travelling wave problem for $\alpha = 0$, i.e., the wave moves parallel to the x axis. For this case the projection, 8-wave, and transport-flux-CT schemes are identical with the base scheme which was verified by the numerical results. The error of the flux-CT scheme is about 1.3 times larger than the error of the base scheme at all the resolutions. The field-CD, flux-CD, and field-CT schemes all give very similar errors, which are about 1.3 to 1.7 times larger than the error of the base scheme at the different resolutions. The standing wave problem is solved exactly by all the schemes for the $\alpha = 0$ case since the fluxes are zero analytically as well as numerically.

6.3.2. The 2D shock tube test. The initial left state is $(\rho, v_{\parallel}, v_{\perp}, p, B_{\parallel}, B_{\perp}) = (1, 10, 0, 20, 5/\sqrt{4\pi}, 5/\sqrt{4\pi})$ and the initial right state is $(1, -10, 0, 1, 5/\sqrt{4\pi}, 5/\sqrt{4\pi})$ for this Riemann problem. The v^z and B^z components are zero. The adiabatic index and the resistivity are $\gamma = 5/3$ and $\eta = 0$. The same problem with its exact solution can be found in [10, 32]. The 2D test with $\alpha = 45^\circ$ was solved with the transport-flux-CT scheme by RMJA and with the projection scheme in [32], and the plotted results look very similar (see also [25]). First I make the comparison for the seven different schemes and the base scheme with a rotation angle $\alpha = \tan^{-1} 2 \approx 63.4^\circ$. Since the magnetic field is uniform initially, for this test problem the initial condition satisfies $\nabla \cdot \mathbf{B} = 0$ for any rotation angle and for any discretization.

The computational domain is a narrow strip with $0 < x < 1$ and $0 < y < 2/N$, and it is resolved by an $N \times 2$ grid. The top and bottom boundaries are of the shifted periodic types (see Subsection 5.5) according to the translational symmetry in the $(-2, 1)$ direction, while the left and right boundaries are fixed according to the initial condition (see Fig. 10). The computation is stopped at time $t_{max} = 0.08 \cos \alpha = 0.08/\sqrt{5}$ before the fast shocks would reach the left and right boundaries. This setup is more economic than using an $N \times N$ grid,

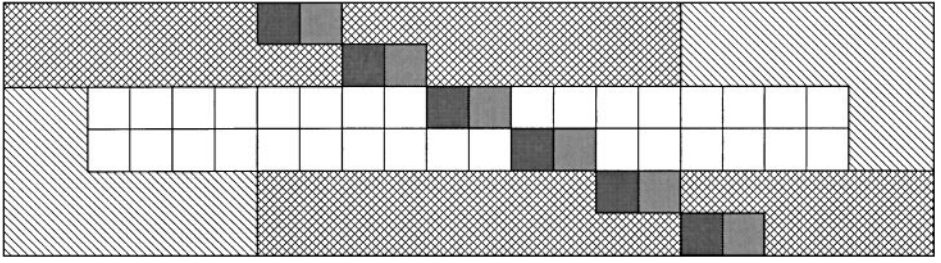


FIG. 10. The grid used for the 2D shock tube problem rotated by $\alpha = \tan^{-1} 2$. The ghost cells on the top and bottom (double shaded area) are copies of the computational domain (middle unshaded part) but shifted to the left and right by four cells. In the rest of the ghost cells (single shaded area) the variables are fixed to the initial left and right states. The flow (dark and light gray squares) has a translational symmetry in the $(-2, 1)$ direction, and the normal vector of the discontinuities point in the $(1, 2)$ direction.

but the results are otherwise identical. In all figures the first row ($j = 1$) of the physical mesh is plotted. The discontinuities look more spread out than in the plots of RMJA, since the final times differ by a factor of $\sqrt{10}$, which means that the effective resolution is approximately 3 times lower for the simulations presented here for the same value of N . In other words, the plots in RMJA are cuts along the $j = k$ diagonal, which is orthogonal to the discontinuities, while the plots in this paper are cuts parallel to the x axis, which is at an angle α relative to the shock normal.

The seven schemes and the base scheme are compared at a resolution $N = 256$. The final time is reached in 170 time steps with $\Delta t = t_{max}/170 \approx 2.1 \times 10^{-4}$. The errors are measured against a high resolution 1D simulation with 1024 grid cells running to $t = 0.08$ in 1600 time steps. The high resolution result is coarsened by a factor of 4 and the vector components are rotated by α to match the low resolution simulations. Both the minmod and MC slope limiters were tried for the base scheme. Formally the errors are slightly smaller for the MC limiter, due to the sharper discontinuities, but there are more pronounced oscillations in the smooth regions. The numerical errors (45) reported in Table III correspond to the minmod limiter. The schemes are listed in the order of their numerical errors averaged for all the primitive variables.

The results show that the non-conservative 8-wave formulation performs the worst for this test. The error is most significant in the parallel magnetic field component, which should be a constant $B_{\parallel} = 5/\sqrt{4\pi} \approx 1.4105$. Figure 11 shows $B_{\parallel} = (B^x + 2B^y)/\sqrt{5}$ for six different schemes. The 8-wave scheme is in error everywhere between the two fast shocks by 3 to 7%.

TABLE III
Numerical Errors in the 2D Shock Tube Test for $\alpha = 63.4^\circ$ and $N = 256$

	$\delta\rho$	δv_{\parallel}	δv_{\perp}	δp	δB_{\parallel}	δB_{\perp}	$\bar{\delta}$
Field-CD	0.0074	0.0175	0.0936	0.0052	0.0046	0.0102	0.0231
Flux-CD	0.0075	0.0175	0.0965	0.0052	0.0036	0.0107	0.0235
Projection	0.0076	0.0177	0.0948	0.0055	0.0062	0.0093	0.0235
Flux-CT	0.0075	0.0176	0.0996	0.0052	0.0016	0.0098	0.0235
Base scheme	0.0075	0.0178	0.1006	0.0055	0.0037	0.0078	0.0238
Tr-flux-CT	0.0075	0.0177	0.1020	0.0054	0.0020	0.0089	0.0239
Field-CT	0.0075	0.0174	0.1214	0.0059	0.0043	0.0178	0.0291
8-wave	0.0076	0.0180	0.1027	0.0056	0.0413	0.0092	0.0307

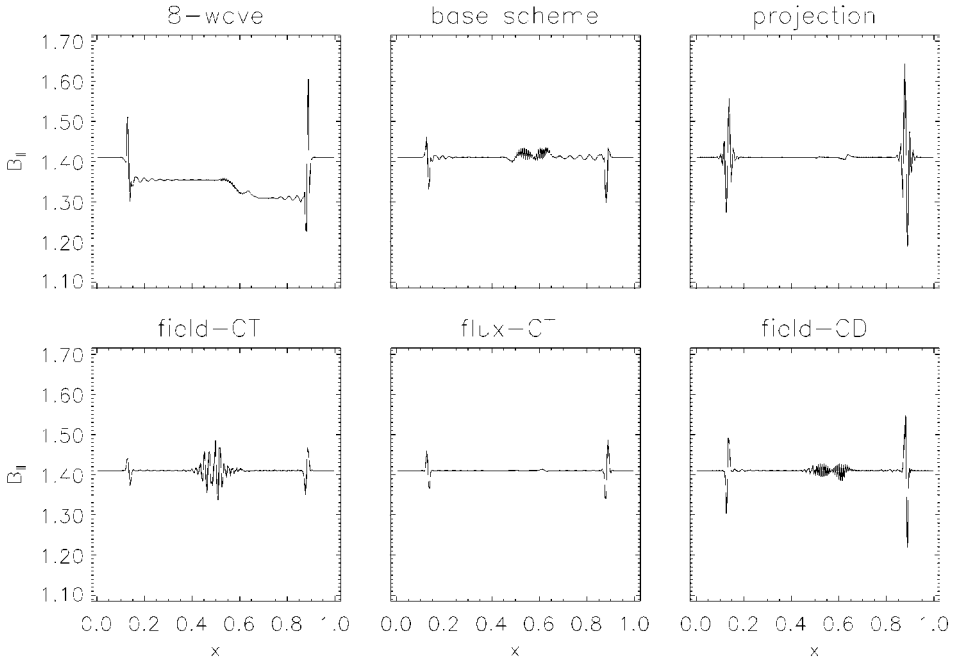


FIG. 11. The parallel component of the magnetic field in the 2D rotated shock tube test is shown for six different schemes. The analytic solution is a uniform value $B_{\parallel} = 5/\sqrt{4\pi}$. The non-conservative 8-wave formulation is in error by several percentage everywhere between the left and right moving fast shocks ($x = 0.1 - 0.9$). The conservative schemes, including the base-scheme (middle top panel), show significant errors close to the discontinuities only.

This error is due to the non-conservative source terms plotted in Fig. 12. When the source terms (and the 8th wave of the Riemann solver) are not included, the base scheme produces correct jumps across the discontinuities as it is shown in the middle top panel in Fig. 11. The conservative schemes also have errors at the discontinuities, but the errors between the discontinuities are smaller and they converge to zero with increased resolution. Figure 13 compares the convergence behaviour of the 8-wave scheme and the field-interpolated central difference schemes by showing B_{\parallel} at $t_{max}/2$ and t_{max} . The results at half time correspond to half the resolution ($N = 128$) due to the self similarity of the solution of Riemann problems. The average deviation from the analytic value of $B_{\parallel} = 5/\sqrt{4\pi}$ does not decrease for the non-conservative 8-wave scheme, while it converges to zero for the conservative field-CD scheme as expected.

To be fair I should say that in many shock tube problems the 8-wave scheme performs well and the conservation across the jumps is satisfactory (see, e.g., the next subsection). The present test problem was selected to demonstrate a potential weakness of non-conservative schemes. On the other hand, it was carefully checked that other choices for the base scheme, e.g., dimensionally unsplit TVD-MUSCL or adding the non-conservative source terms by operator splitting, do not fix or diminish the problem. It was also checked that the error is not a consequence of the initial startup errors: when the simulation is continued with the 8-wave scheme starting from the divergence-free output of the projection or field-CD scheme at an intermediate time, the incorrect jump in the parallel magnetic field appears with the same magnitude as in Fig. 12.

Among the conservative schemes, the field-CT scheme is the least accurate due to large oscillations behind the slow rarefaction wave (see the bottom left panel in Fig. 11). It was

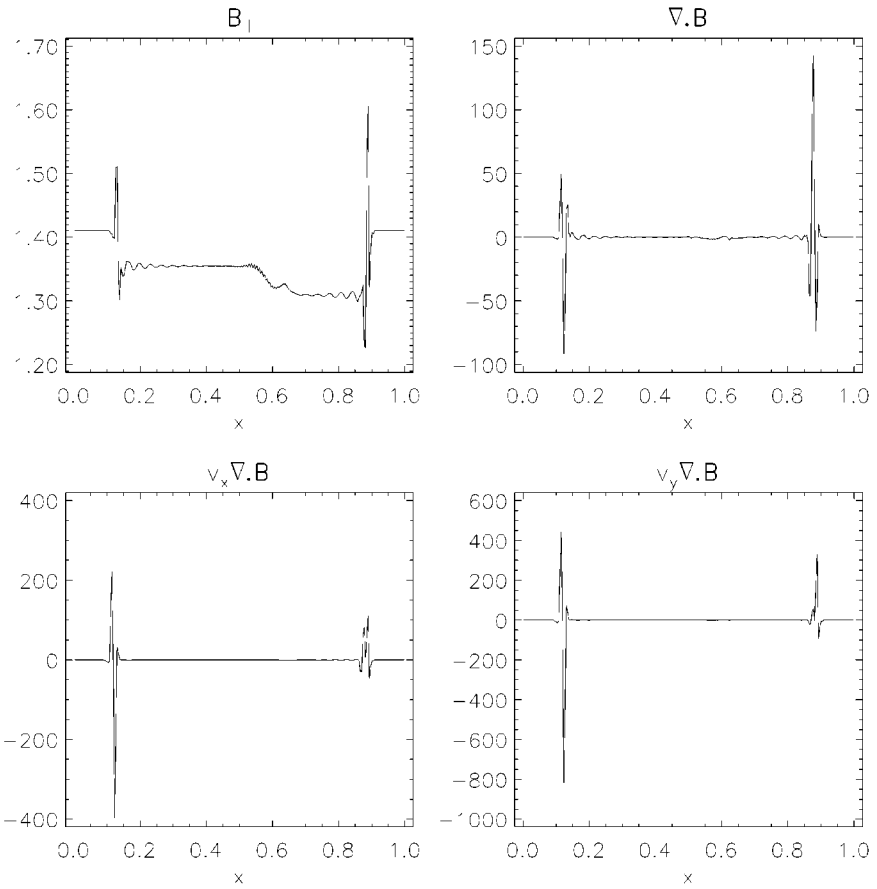


FIG. 12. In the rotated shock tube problem, the incorrect jumps of the parallel magnetic field (top left) for the 8-wave formulation are due to the source terms (bottom left and right) in the non-conservative form of the induction equation (13). The source terms are proportional to the numerical value of $\nabla \cdot \mathbf{B}$ (top right), which has large oscillations at the discontinuities independent of the resolution.

checked that these oscillations do not reduce if an entropy fix (the same as in RMJA) was used, or if the time step was reduced by a factor of 2. The rest of the schemes (top six rows in Table III) can be ordered differently depending which variable we take for comparing the errors. The relative errors are largest in the orthogonal velocity component since $|v_{\perp}|$ is much smaller than the Cartesian components $|v^x|$ and $|v^y|$, but the numerical errors in v^x and v^y do not cancel for $v_{\perp} = (v^y - 2v^x)/\sqrt{5}$. The gap between the best six and worst two schemes remains significant even if the error δv_{\perp} is not taken into account. The magnetic field is most accurate for the flux- and transport-flux-CT schemes. In terms of the average error, the most accurate algorithm for this problem happens to be the simple field-CD scheme (see Fig. 14), although one should not take the differences between the top six schemes very seriously. Despite the reservations emphasised by DW, the projection scheme solves this superfast flow (the velocity exceeds the fast magnetosonic speed by a factor of 4.2) significantly more accurately than the field-CT scheme proposed by the same authors. This is a practical demonstration of the theoretical arguments discussed in Subsection 5.3.

It is interesting to check the numerical value of $\nabla \cdot \mathbf{B}$ for the various schemes. Table IV shows the maximum and average values of $|\nabla \cdot \mathbf{B}|$ according to both the central difference

TABLE IV
Divergence B in the 2D Rotated Shock Tube Test

	$ \nabla \cdot \mathbf{B}_{j,k} $		$ \nabla \cdot \mathbf{B}_{j+1/2,k+1/2} $	
	Max	Avrg	Max	Avrg
Base scheme	141.5	3.43	48.9	3.27
8-wave	142.5	3.62	57.0	1.91
Projection	0.3	0.01	130.9	4.73
Field-CD	10^{-12}	10^{-13}	84.2	3.81
Flux-CD	10^{-12}	10^{-13}	68.5	3.91
Field-CT	65.9	5.63	10^{-12}	10^{-13}
Flux-CT	73.5	2.09	10^{-12}	10^{-13}
Tr-flux-CT	102.8	2.95	10^{-12}	10^{-13}

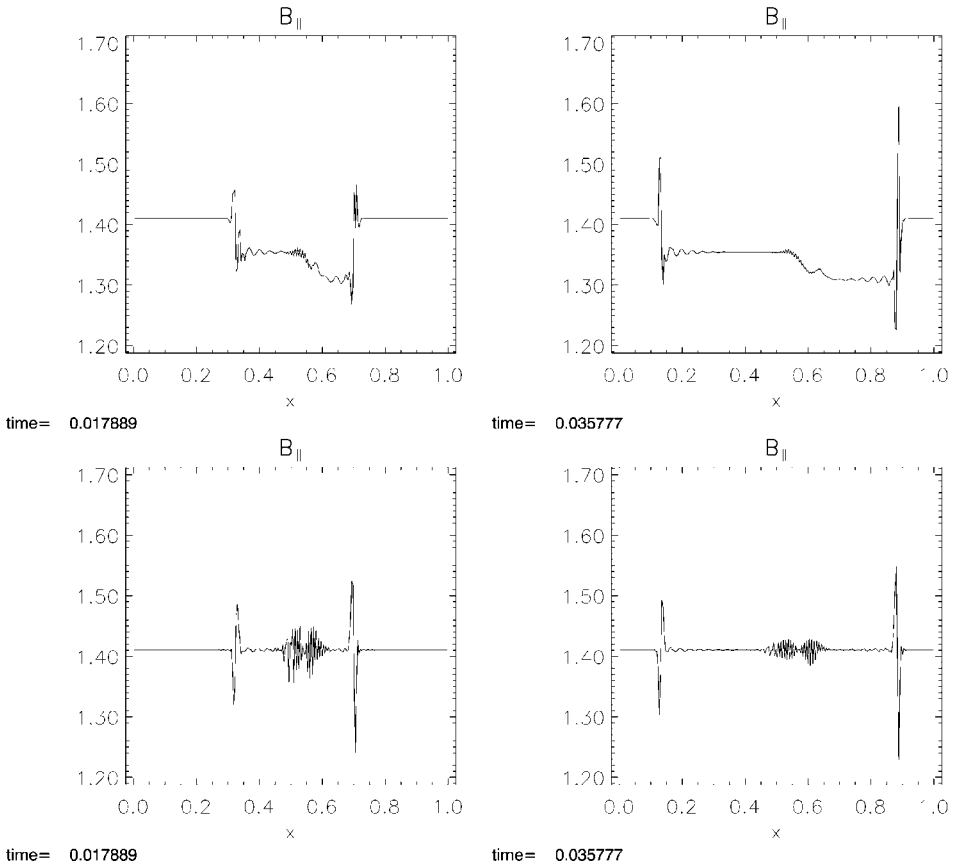


FIG. 13. The convergence behaviour of the parallel component of the magnetic field is shown for the non-conservative 8-wave (top) and the conservative field-CD (bottom) schemes for the 2D rotated shock tube test. The plots at half time (left) correspond to a resolution of 128 points, while the results at the final time make use of the full resolution of 256 grid cells. The results by the non-conservative method do not converge to the correct uniform solution, while the conservative scheme converges to $B_{\parallel} = 5/\sqrt{4\pi}$ everywhere except for a fixed number of cells in the vicinity of the discontinuities.

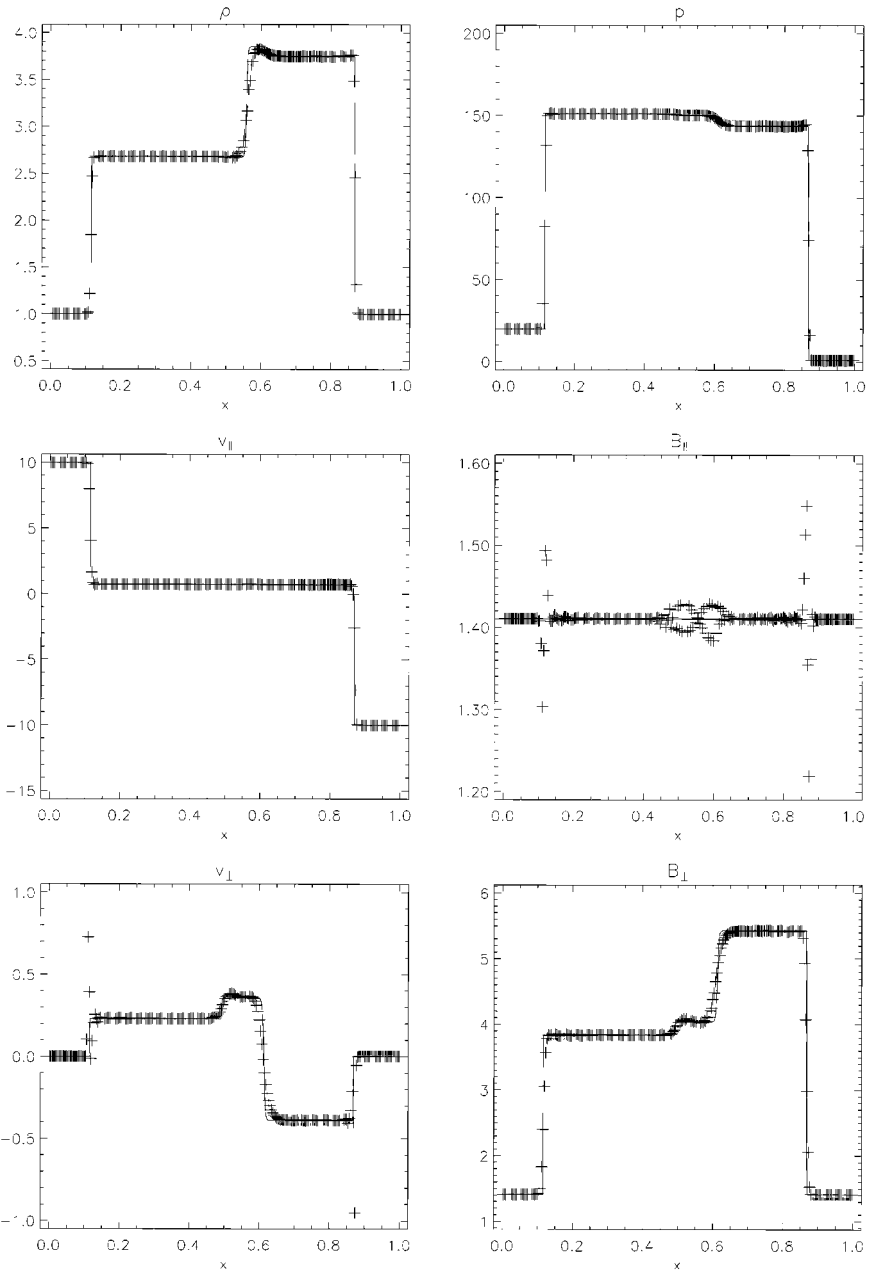


FIG. 14. The solution of the 2D rotated shock tube problem by the field-CD scheme (symbols) on a 256×2 grid. For comparison, the non-rotated 1D solution with 1024 grid cells is also plotted (line).

(26) and the cell corner centered (27) definitions for all seven schemes and the base scheme. As expected, the central difference definition for the CD schemes and, similarly, the cell corner centered discretization for the CT schemes are around the round off error 10^{-12} . The projection scheme keeps the cell centered discretization below 0.3 using 20 iterations of the conjugate gradient solver in every time step. It was checked that the results hardly change if the Poisson problem was solved much more accurately with $\epsilon = 0.01$, but of course such

TABLE V
Average Errors in the 2D Rotated Shock Tube Test

	$\alpha = 63.4^\circ$		$\alpha = 45^\circ$	
	$\bar{\delta}_{128}$	$\bar{\delta}_{256}$	$\bar{\delta}_{128}$	$\bar{\delta}_{256}$
Field-CD	0.0345	0.0231	0.0249	0.0132
Projection	0.0351	0.0235	0.0238	0.0130
Flux-CT	0.0336	0.0235	0.0253	0.0134
Flux-CD	0.0341	0.0235	0.0253	0.0134
Tr-flux-CT	0.0340	0.0239	0.0258	0.0140
Base scheme	0.0336	0.0238	0.0376	0.0258
Field-CT	0.0437	0.0291	0.0316	0.0165
8-wave	0.0413	0.0307	0.0374	0.0264

a precision requires more iterations. It is quite interesting to see that for all the six schemes (3rd to 8th rows in the Table IV) that keep $\nabla \cdot \mathbf{B}$ very small in one discretization, in the *other* discretization $\nabla \cdot \mathbf{B}$ is not at all small when compared to the 8-wave scheme or the base scheme. There seems to be no straightforward relationship between the overall accuracy of a method and its ability to keep $\nabla \cdot \mathbf{B}$ small in some particular discretization.

The schemes were also compared at half the resolution ($N = 128$) and the overall picture remains the same: the 8-wave and the field-CT schemes are significantly less accurate than the other four schemes. The convergence rate is around first order for all the primitive variables except for the orthogonal velocity component, for which the errors diminish by 10 to 20% only as the resolution goes from $N = 128$ to 256.

I repeated the test problem for the rotation angle $\alpha = 45^\circ$ as well (same as used by RMJA) with $t_{max} = 0.08/\sqrt{2}$. For this special choice of angle, the divergence of \mathbf{B} is zero to machine accuracy for all CT and CD schemes in both the central difference (26) and the cell corner centered (27) discretizations and the uniform parallel component of the magnetic field $B_{\parallel} = 5/\sqrt{4\pi}$ is also conserved accurately. The 8-wave scheme produces incorrect jump conditions, and it converges to a B_{\parallel} which is in error by 5% to 10% between the fast shock waves. Table V summarizes the average errors for rotation angles $\alpha = 63.4^\circ$ and 45° and resolutions $N = 128$ and 256. In all four cases there is a gap between the five most and the two least accurate methods, while the base scheme seems to do the problem with $\alpha = 63.4^\circ$ better than with $\alpha = 45^\circ$. Comparison of values of $\bar{\delta}_{128}$ and $\bar{\delta}_{256}$ indicates an approximately first order convergence rate for the conservative schemes for $\alpha = 45^\circ$ and somewhat worse for $\alpha = 63.4^\circ$ due to the error in v_{\perp} .

6.3.3. The 2.5D shock tube test. This rotated shock tube problem is a 2.5D test since all three components of the velocity and magnetic fields are non-zero. The initial left and right states of this Riemann problem are $(\rho, v_{\parallel}, v_{\perp}, v_z, p, B_{\parallel}, B_{\perp}, B_z) = (1.08, 1.2, 0.01, 0.5, 0.95, 2/\sqrt{4\pi}, 3.6/\sqrt{4\pi}, 2/\sqrt{4\pi})$ and $(1, 0, 0, 0, 1, 2/\sqrt{4\pi}, 4/\sqrt{4\pi}, 2/\sqrt{4\pi})$, and $\gamma = 5/3$, $\eta = 0$. The same Riemann problem with its exact solution can be found in [10, 32]. Since the initial condition contains a jump in the magnetic field, this test is easiest to do with a rotation angle $\alpha = 45^\circ$ which ensures $\nabla \cdot \mathbf{B} = 0$ both in the cell centered (26) and the corner centered (27) discretizations. This test is identical with RMJA for the transport-flux-CT scheme and with [32] for the projection scheme except for the final time, which is $t_{max} = 0.2/\sqrt{2}$, exactly half of the value used by RMJA. This test problem is also done

TABLE VI
Convergence of Average Errors in the 2.5D Shock Tube Test

	Minmod		MC limiter	
	$\bar{\delta}_{128}$	$\bar{\delta}_{256}$	$\bar{\delta}_{128}$	$\bar{\delta}_{256}$
Projection	0.0182	0.0111	0.0129	0.0074
8-wave	0.0190	0.0119	0.0131	0.0071
Tr-flux-CT	0.0188	0.0114	0.0156	0.0093
Field-CD	0.0190	0.0115	0.0156	0.0093
Flux-CD/CT	0.0197	0.0120	0.0171	0.0107
Base scheme	0.0206	0.0124	0.0187	0.0121
Field-CT	0.0213	0.0134	0.0192	0.0126

in [25]. Again an $N \times 2$ grid is used with $N = 256$; thus the effective resolution is half of RMJA's. The time step is $\Delta t = t_{max}/120$. The high resolution 1D solution is obtained with the base scheme on a $N = 1024$ grid at $t = 0.2$ using $\Delta t = 0.00025$.

For this test case the monotonic central limiter is clearly superior to the minmod limiter since it gives smaller errors due to the sharper discontinuities and the oscillations are very small. The average errors $\bar{\delta}$ are shown for the seven schemes and the base scheme at the resolutions $N = 128$ and 256 in Table VI. Although the special choice of α should favour the CT and CD algorithms (since $B_{||}$ is exactly conserved by them) the average error is the smallest for the 8-wave and projection schemes. For this test problem the non-conservative source terms of the 8-wave scheme do not introduce a significant error. In Fig. 15 the results of the 8-wave scheme are shown together with the reference high resolution solution. The field-CT scheme gives the worst result: its average error is approximately 1.5 times larger than that of the most accurate schemes.

6.4. Orszag–Tang Vortex

The Orszag–Tang vortex problem [28] has been used in many papers [11, 12, 25, 35, 44, 50] as a two-dimensional numerical test for MHD codes, although the choices for the length and time units differ. Here I use the same normalization as in [44]. The computational domain is a square with $0 < x, y < 2\pi$ and periodic boundary conditions. The initial vortex structure is defined by $\rho = 25/9$, $v_x = -\sin y$, $v_y = \sin x$, $B_x = -\sin y$, $B_y = \sin 2x$, $p = 5/3$, $v_z = 0$, $B_z = 0$, and the equation parameters are $\gamma = 5/3$ and $\eta = 0$. In the numerical initial condition $\gamma = p = 1.667$ and $\rho = 2.778$ were used, but for the coordinates a double precision value is taken for 2π to make the periodicity accurate.

Three different resolutions are taken for the $N \times N$ grid: $N = 50, 100$, and 200. The numerical errors are calculated relative to “high resolution” results with $N = 400$. Even at this high resolution the numerical results differ somewhat depending on the numerical scheme. To make the comparison fair, two high resolution results were obtained with the projection and the field-CT schemes, and the numerical errors reported in Table VII are the averages of the errors relative to the two high resolution runs. The time step is $\Delta t = 2/N$ for all the simulations.

The Orszag–Tang vortex problem starts from smooth initial data, but gradually the flow becomes very complex as expected from a transition towards turbulence. At time $t = 1$ the flow is still quite smooth, although some discontinuities are already present. The accuracy of

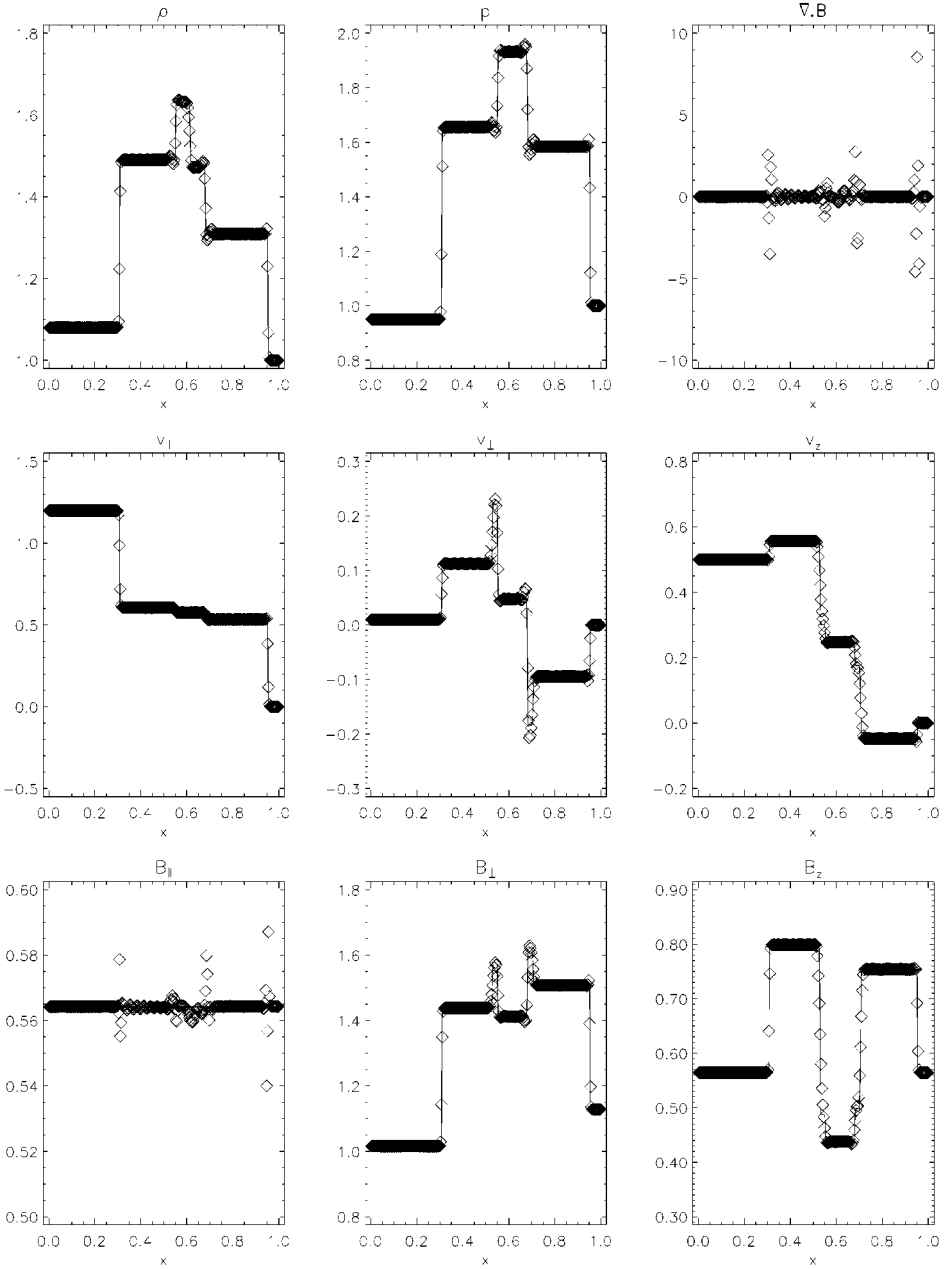


FIG. 15. The solution of the 2.5D rotated shock tube problem by the 8-wave scheme (symbols) on a 256×2 grid. For comparison, the non-rotated 1D solution with 1024 grid cells is also plotted (line).

the schemes for dominantly smooth problems can be compared at this time. Table VII lists the average relative errors for the primitive variables for the three resolutions. The errors are more or less evenly distributed among the primitive variables and the ordering of the schemes is essentially independent of which primitive variable the errors are measured by. All seven schemes and the base scheme converge with a convergence rate of approximately 1.6, which is worse than the second order accuracy expected for completely smooth flow, but better than the first order accuracy obtained in dominantly discontinuous problems. The

TABLE VII
Convergence of Averaged Errors in the Orszag–Tang Test

	$t = 1$				$t = 3.14$		
	$\bar{\delta}_{50}$	$\bar{\delta}_{100}$	$\bar{\delta}_{200}$		$\bar{\delta}_{50}$	$\bar{\delta}_{100}$	$\bar{\delta}_{200}$
Field-CD	0.0250	0.0085	0.0026	Field-CD	0.1150	0.0617	0.0300
Field-CT	0.0284	0.0096	0.0029	Projection	0.1280	0.0709	0.0340
Projection	0.0287	0.0109	0.0035	Field-CT	0.1393	0.0720	0.0355
Flux-CT	0.0321	0.0114	0.0035	Flux-CT	0.1352	0.0737	0.0358
8-wave	0.0305	0.0119	0.0043	Flux-CD	0.1380	0.0775	0.0373
Flux-CD	0.0347	0.0122	0.0037	Tr-flux-CT	0.1527	0.0837	0.0439
Base scheme	0.0324	0.0128	0.0044	8-wave	0.1420	0.0867	0.0478
Tr-flux-CT	0.0349	0.0134	0.0045	Base scheme	0.1784	0.1097	0.0705 ^a

^a Obtained with the minmod limiter.

averaged relative errors $\bar{\delta}$ of the most accurate field-CD and the least accurate transport-flux-CT schemes differ by about a factor of 1.5.

The situation changes a lot when the schemes are compared at $t = 3.14$, which is approximately the same time for which the different quantities are plotted in [11, 12, 25, 35, 44, 50]. (I note that Balsara [2] ran an isothermal MHD version of this test problem to time $t = 3$ using the same distance unit as here, but their time unit, which is presumably smaller than here, was not specified, so it is difficult to make a comparison with his results.) The average numerical errors are reported in Table VII. The errors per primitive variable have similar values as $\bar{\delta}$ and they all show the same order among the schemes. The base scheme fails for the Orszag–Tang problem at resolution $N = 200$ due to accumulation of errors that eventually result in non-physical states. A solution could only be obtained with the minmod limiter.

There are lots of things that can be read from the table. The convergence rate dropped to 1, which shows that the integrated errors defined in (45) are dominated by the errors at the discontinuities. For the same reason, the errors are much larger at $t = 3.14$ than they were at $t = 1$. The base scheme is considerably less accurate than the other schemes, even for the resolutions where it succeeded with the MC limiter. The projection scheme became second best, while the simplest field-CD scheme kept its leading position.

The qualitative differences in resolution can be appreciated in the six gray scale images of temperature in Fig. 16. I plot temperature, since it is a good indicator of shocks as well as contact discontinuities. The reference high resolution solution (bottom right) was obtained with the projection scheme on a 400×400 grid. The other five plots are results of five different schemes with 100×100 resolution. Only the left half of the computational domain is shown since the right half is symmetric to the center point $x = y = \pi$. Looking at the images, the field-CD and field-CT results are obviously sharper than the other three solutions. Only these two schemes show clearly the sharp dark (cold) feature between $x = y = 1$ and $x = 0.5, y = 2$. The feature can hardly be seen in the solution from the projection scheme, and it is completely smeared out in the 8-wave and flux-CT results. Although the solution with the field-CT scheme looks sharp, it contains spurious oscillations around $x = 0, y = 3$, some dark spots around $x = y = 3$, and white spots around $x = 3, y = 6$, which should not be there according to the high resolution solution. To a much lesser extent these spurious features can also be detected in the field-CD

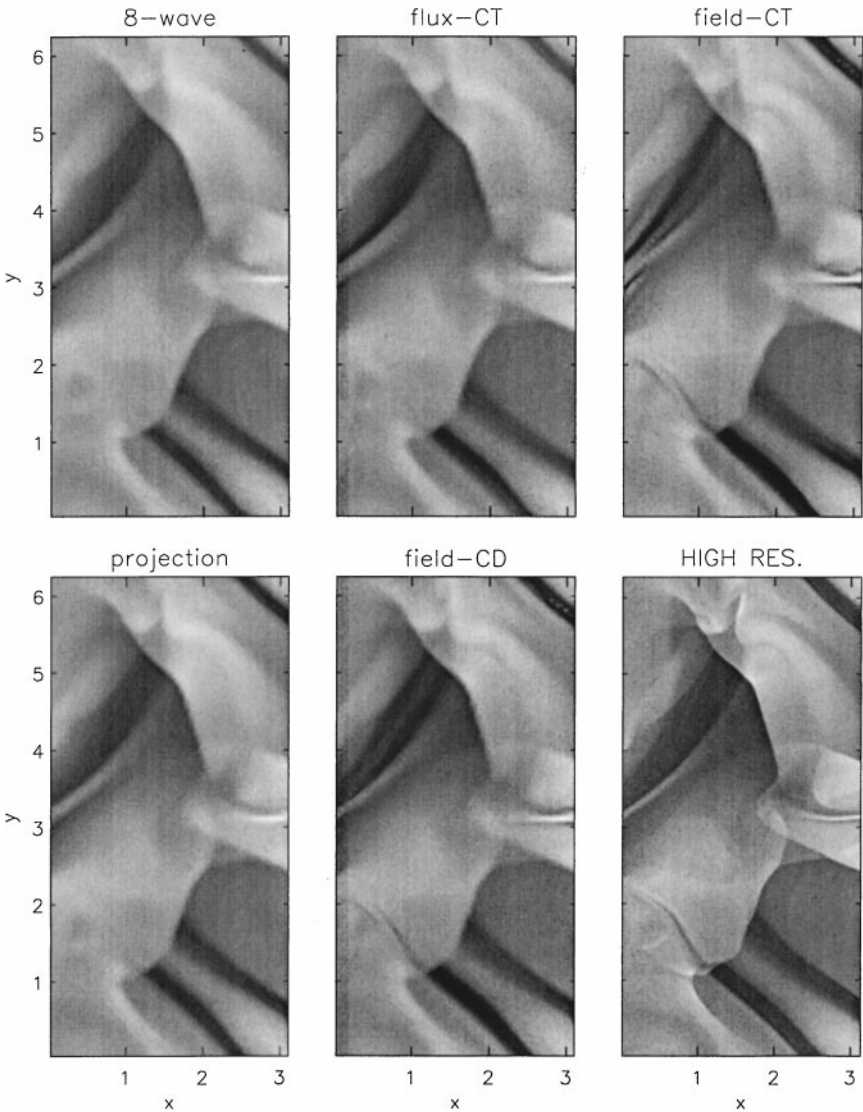


FIG. 16. The temperature distribution in the Orszag–Tang vortex problem. Only the left half of the computational domain is shown, the other half is symmetric. The five schemes are compared at a 100×100 resolution. The reference high resolution solution (bottom right panel) was computed on a 400×400 grid with the projection scheme. The temperature range is from 0.15 (black) to 1.24 (white).

result. Although the projection scheme does not look much sharper than the 8-wave and flux-interpolated schemes, according to the quantitative measure of error it is the second most accurate algorithm for the temperature. The average errors (measured against two high resolution solutions obtained with the projection and field-CT methods) are $\delta T = 0.0323, 0.0330, 0.0335, 0.0357, 0.0373, 0.0385, 0.0416, \text{ and } 0.0463$ for the field-CD, projection, flux-CT, flux-CD, 8-wave, transport-flux-CT, field-CT, and base schemes, respectively.

6.5. Cloud-Shock Interaction

This problem models the disruption of a high density cloud by a strong shock wave. The test problem is taken from DW [12] and it is presented here to test the different schemes

on highly superfast flows. The computational domain is $0 < x, y < 1$ resolved by a uniform $N \times N$ grid. The initial condition contains a discontinuity parallel to the y axis at $x = 0.6$ with the left and right states $(\rho, v_x, v_y, v_z, p, B_x, B_y, B_z) = (3.86859, 0, 0, 0, 167.345, 0, 2.1826182, -2.1826182)$ and $(1, -11.2536, 0, 0, 1, 0, 0.56418958, 0.56418958)$ with $\gamma = 5/3, \eta = 0$. The discontinuity is a combination of a fast shock wave and a rotational discontinuity in B_z . The rotational discontinuity has no effect on the evolution of other flow variables. The circular cloud is located at $x = 0.8, y = 0.5$ with a radius 0.15, density $\rho = 10$, and pressure $p = 1$ in hydrostatic equilibrium with the surrounding plasma. There is a fixed boundary condition on the right at $y = 1$ due to the supersonic inflow, while the other boundaries are approximately open using the zero-gradient boundary condition.

It was found that the dimensionally split one step TVD scheme can easily fail due to non-physical states produced during the violent collision of the shock and the cloud even when the minmod limiter and an entropy fix were used. Although the difficulties can be avoided by significantly reducing the time step and/or by making the edge of the cloud smoother, I decided to use another base scheme, the two step TVD-MUSCL scheme with a Hancock predictor step, with no dimensional splitting, and with the monotized central slope limiters applied on the primitive variables. This base scheme is not compatible with the transport-flux-CT algorithm, so that v_z is not tested. The time step is adjusted dynamically so that the Courant number never exceeds $C = 0.6$ and the last time step reaches exactly the final time $t_{max} = 0.06$. Using this base scheme the test problem could be solved successfully with all the tested schemes at all the tested resolutions with two exceptions. The field-CT scheme failed at higher resolutions just a few steps before completion, but a subtle change of averaging the electric field instead of the magnetic and velocity fields fixed this problem. This minor modification does not change the essential characteristics of the scheme. The base scheme has also failed for the $N = 200$ resolution, which could only be done by using the minmod limiter instead of the sharper MC limiter.

The simulations were carried out at resolutions $N = 50, 100, \text{ and } 200$. Two reference solutions were obtained with the projection and the field-CD schemes at a resolution $N = 400$. The results of the projection scheme are shown in Fig. 17 which should be compared with Figs. 18 and 19 in [12]. The magnetic field solutions look very similar if we take into account that DW plot more contourlines in the post shock region, suppress contourlines in the preshock region, and cut off the edges of the simulation domain. The density plots also compare well, although certain details, like the two “eyes” visible in DW’s Fig. 18 at $x = 0.4, y = 0.4$ and 0.6 do not show up in Fig. 17 or in any of the results obtained by the other schemes. This may be due to the color coding of the DW plot.

All the schemes perform very similarly for this problem; their averaged numerical errors differ by less than 5% from $\bar{\delta}_{50} = 0.2, \bar{\delta}_{100} = 0.15, \text{ and } \bar{\delta}_{200} = 0.08$ and the errors of the individual primitive variables also agree within 10%. The only exception is the base scheme at $N = 200$ resolution, where $\bar{\delta}_{200} = 0.14$ due to the use of the minmod limiter. The relative errors are highest for the v_z and B_x variables which are zero initially. The convergence rate is approximately first order between $N = 100$ and 200 which is expected for a dominantly discontinuous problem.

6.6. Rotor

This test problem is taken from BS. The computational domain is a unit square $0 < x, y < 1$ resolved by $N \times N$ grid cells. The initial thermal pressure and magnetic field are uniform

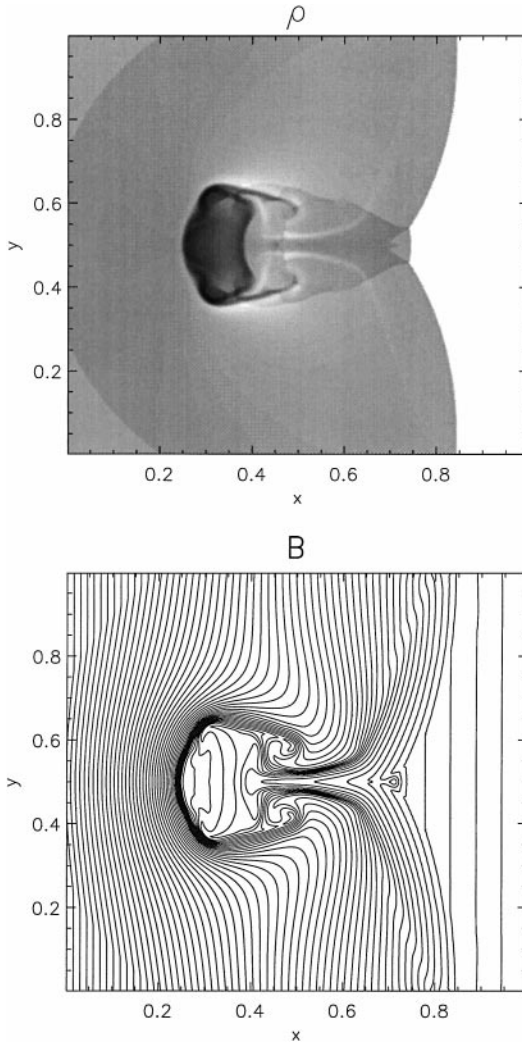


FIG. 17. The magnetic field lines and the density distribution in the cloud-shock interaction problem solved by the projection scheme on a 400×400 grid. The density range goes from 1 (white) to 44 (black) with a logarithmic gray scale.

with $B_y = 0$. There is a dense rotating disk of fluid with $\rho = 10$, $v_x = -v_0(y - 0.5)/r_0$, and $v_y = v_0(x - 0.5)/r_0$ out to a radial distance $r < r_0$, where $r = [(x - 0.5)^2 + (y - 0.5)^2]^{1/2}$ is measured from the center point and $r_0 = 0.1$. The ambient fluid is at rest with $\rho = 1$ and $v_x = v_y = 0$ for $r > r_1 = 0.115$. The fluid between the rotating and the ambient fluid at $r_0 < r < r_1$ has linear density and angular speed profiles with $\rho = 1 + 9f$, $v_x = -fv_0(y - 0.5)/r$, and $v_y = fv_0(x - 0.5)/r$, where $f = (r_1 - r)/(r_1 - r_0)$ is a “taper” function, which helps to reduce initial transients. Note that the rotor is not in equilibrium, since the centrifugal forces are not balanced. The magnetic field, as it winds up, will confine the rotating dense fluid into an oblate shape. There is no resistivity, $\eta = 0$.

By mistake the final time and the plots in BS do not correspond to the initial condition described in the text (BS, private communication). First I will solve the problem as defined in the text of BS: $v_0 = 2$, $p = 1$, $B_x = 5/\sqrt{4\pi}$, and adiabatic index $\gamma = 1.4$. The final time

$t_{max} = 0.15$ will be used in this *first rotor problem*, when the flow looks similar, although not identical, to the plots of BS. The *second rotor problem*, which was used to obtain the plots in BS, is defined by $v_0 = 1$, $p = 0.5$, $B_x = 2.5/\sqrt{4\pi}$, and adiabatic index $\gamma = 5/3$. For this problem the final time is $t_{max} = 0.295$ as in BS. (I note that Londrillo and Del Zanna [25] solve the first rotor problem with $r_0 = r_1 = 0.1$ and a final time $t = 0.18$.)

For the first rotor problem, experiments with the one step TVD base scheme showed that many of the algorithms fail due to negative pressure; thus the more robust dimensionally unsplit TVD-MUSCL base scheme is used. The MC limiter is applied on the primitive variables. This base scheme excludes the transport-flux-CT algorithm from the test. The remaining six schemes and the base scheme were tested at resolutions $N = 50, 100$, and 200 . The reference solutions were obtained with the projection and flux-CT schemes (see Fig. 18) with $N = 400$. In all runs, the time step is dynamically set so that the Courant number does not exceed 0.6 and the final time is reached exactly. The errors, averaged relative to the two reference solutions, are listed in Table VIII on the left side.

The second rotor problem, which has a factor of two higher thermal pressure relative to magnetic and dynamic pressures, could be solved successfully using the dimensionally

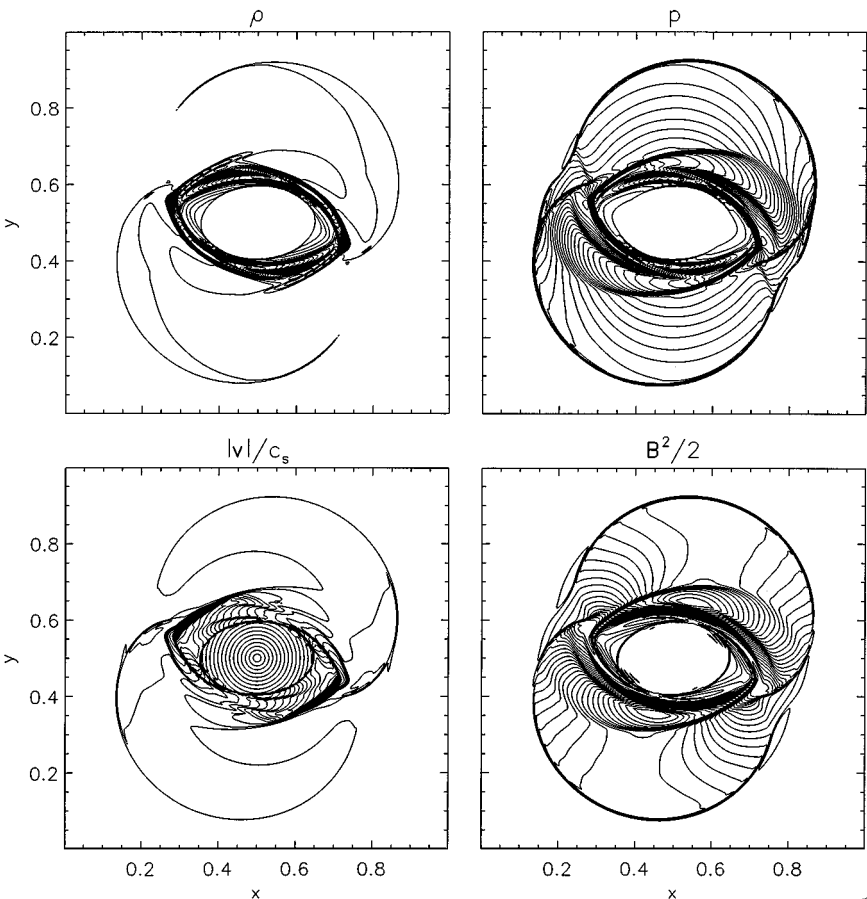


FIG. 18. The density, thermal pressure, Mach number, and magnetic pressure, at $t = 0.15$ for the first rotor problem. The solution was obtained by the flux-CT scheme on a 400×400 grid. The 30 contourlines are shown for the ranges $0.483 < \rho < 12.95$, $0.0202 < p < 2.008$, $0 < |v|/c_s < 8.18$, and $0.0177 < B^2/2 < 2.642$, respectively.

TABLE VIII
Convergence of Averaged Errors in the Rotor Tests

First rotor test with $p = 1$			Second rotor test with $p = 0.5$				
	$\bar{\delta}_{50}$	$\bar{\delta}_{100}$	$\bar{\delta}_{200}$		$\bar{\delta}_{50}$	$\bar{\delta}_{100}$	$\bar{\delta}_{200}$
Projection	0.1145	0.0603	0.0276	Projection	0.1146	0.0625	0.0324
8-wave	0.1152	0.0621	0.0285	8-wave	0.1153	0.0657	0.0354
Flux-CT	0.1191	0.0624	0.0298	Field-CD	0.1250	0.0652	0.0337
Base scheme	0.1185	0.0637	0.0329	Base scheme	0.1176	0.0667	0.0363
Field-CD	0.1340	0.0728	0.0354	Flux-CT	0.1218	0.0682	0.0369
Flux-CD	0.1344	0.0716	0.0355	Flux-CD	0.1283	0.0696	0.0361
Field-CT	0.1537	0.0893	0.0488	Tr-flux-CT	0.1195	0.0708	0.0491 ^a
				Field-CT	0.1404	0.0777	0.0453

^a Obtained with the minmod limiter.

split one step TVD base scheme using the MC limiter. The only exception is the transport-flux-CT scheme at resolution $N = 200$, where the minmod limiter had to be used to avoid break down due to unphysical states. Also, the reference high resolution $N = 400$ solutions were obtained with the projection and the field-CD schemes using the TVD-MUSCL base scheme, since the one-step TVD scheme with the MC limiter failed for this resolution (using the minmod limiter would probably help, but it would degrade the accuracy of the reference solutions). The same quantities that were plotted by BS in their Fig. 2 are shown for the high resolution result obtained with the projection scheme in Fig. 19. There is an excellent agreement. The relative errors of the various schemes at different grid resolutions are listed in Table VIII on the right.

For both rotor problems, all schemes converge at an approximately first order rate. The projection scheme and the field-CT schemes are the most and least accurate among the compared methods. The ratio of their relative errors is around 1.5 and 1.3 for the first and second tests, respectively. It should be noted that the average errors do not reflect all the properties of the results. For example, many of the schemes produce undershoots in pressure and the corresponding sound speed, which reflect as spurious peaks in the Mach number $|\mathbf{v}|/c_s$. The pressure undershoots hardly influence the error δp . To avoid such undershoots, one may prefer to use an energy correction like (40). For the first rotor problem, a test with the field-CD scheme at $N = 200$ resolution showed that the energy correction removes the pressure undershoots while the other variables or the overall accuracy hardly change. Therefore the second rotor problem was solved with the energy correction for all the schemes and resolutions. In all the runs, the total energy conservation is violated by less than 0.4% during the whole computation due to the correction.

To get an impression of qualitative differences, contourplots of the Mach number in the second rotor problem are shown for seven different schemes together with the base scheme and a high resolution reference solution in Fig. 20. The central part shows significant distortion of the circularly rotating velocity field for the base scheme and the field-CT schemes. The error looks similar to the one shown by BS in Fig. 3 for their dimensionally split base scheme. BS argue that the error is related to the error in the divergence of the magnetic field, but the simulations presented here do not support this explanation. The field-CT scheme, which maintains $\nabla \cdot \mathbf{B} = 0$ to machine accuracy in the CT discretization,

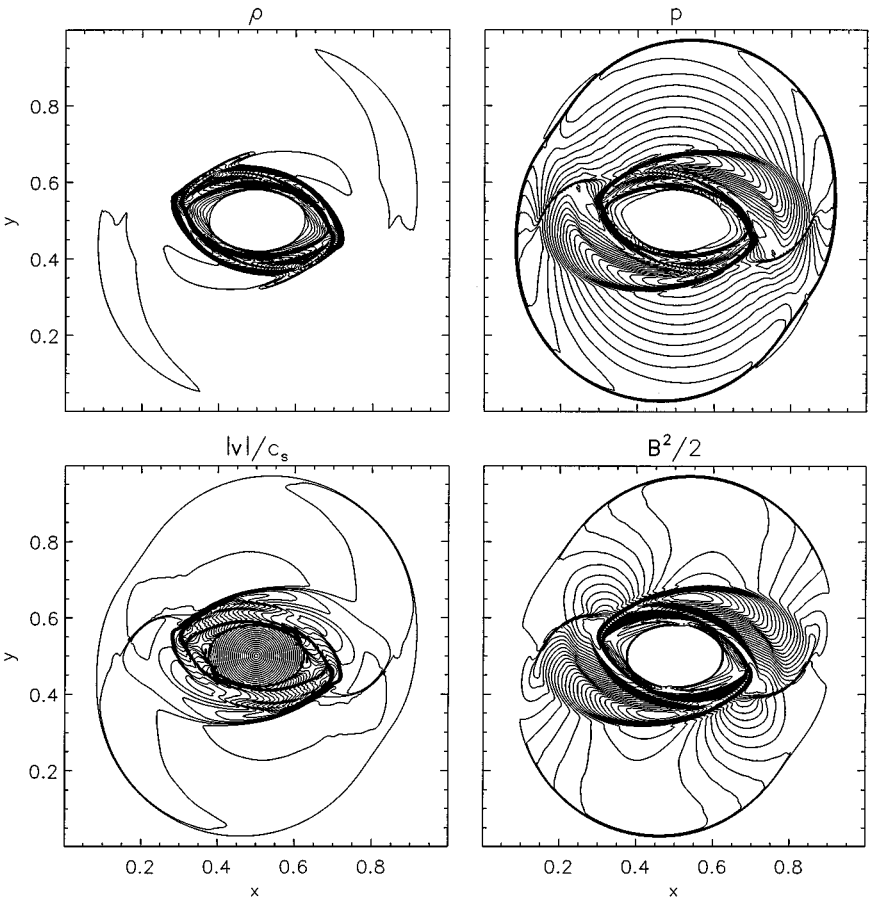


FIG. 19. The density, thermal pressure, Mach number, and magnetic pressure at $t = 0.295$ for the second rotor problem. The solution was obtained by the projection scheme on a 400×400 grid. The 30 contourlines are shown for the ranges $0.532 < \rho < 10.83$, $0.007 < p < 0.776$, $0 < |v|/c_s < 3.64$, and $0.007 < B^2/2 < 0.702$, respectively.

shows very distorted velocity contours, while the 8-wave scheme, which has finite errors in $\nabla \cdot \mathbf{B}$, does not suffer from this problem.

7. CONCLUSIONS

The main points of the algorithmic sections are the following:

- The 8-wave formulation is non-conservative which may cause incorrect jump conditions occasionally.
- Staggered variables can be eliminated from all the constrained transport type algorithms; thus the CT schemes can be viewed as finite volume discretizations.
- The new central difference based schemes are considerably simpler than the analogous constrained transport type methods.
- The field-interpolated CD scheme does not require spatial interpolation.
- The CT and CD schemes can be generalized to arbitrary curvilinear grids, to axial symmetry, and to resistive MHD.

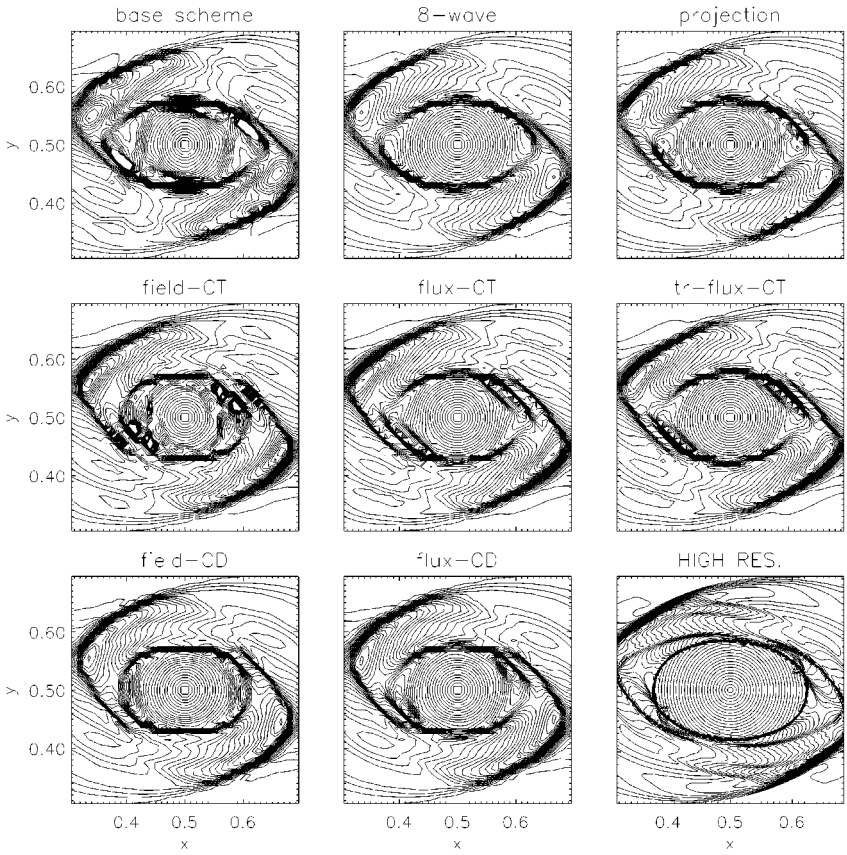


FIG. 20. The Mach number $|v|/c_s$ for the second rotor problem in the central part of the computational domain. The seven schemes and the base scheme are compared at a 100×100 resolution. The reference high resolution solution (bottom right panel) was computed on a 400×400 grid with the projection scheme. The 30 contourlines are shown for the Mach number ranging from 0 to 3.3.

- The projection scheme is consistent and has the same order of accuracy as the base scheme even for discontinuous (e.g., superfast) flows.
- The projection scheme can be implemented in an efficient, parallelizable, and flexible way using iterative Poisson solvers.

Let us summarize the properties of the seven schemes: the 8-wave formulation, the field- and the (transport)-flux-interpolated CT and CD schemes, and the projection method. All seven schemes can be regarded as some modification of a *base scheme*, which is assumed to be second order accurate in space and time for smooth solutions and conservative in a finite volume sense, so that discontinuities are handled properly. All seven schemes maintain the second order accuracy for smooth solutions. The 8-wave formulation spoils conservation, the other six schemes are conservative. The 8-wave formulation conserves $\nabla \cdot \mathbf{B}$ to the accuracy of the truncation error, the CT and CD algorithms conserve $\nabla \cdot \mathbf{B}$ in some particular discretization down to round off errors, while the projection scheme removes the divergence of the magnetic field to the accuracy of the Poisson solver. It is important to note that the CT schemes maintain $\nabla \cdot \mathbf{B} = 0$ in a cell corner centered sense (27) while the CD and the projection methods use a more natural cell centered discretization (26). Due to the

differences in handling $\nabla \cdot \mathbf{B}$, the schemes are more or less sensitive to discretization errors in the boundary and initial conditions. The projection scheme removes the errors from the initial condition, and errors due to the boundary conditions influence only the edges of the computational domain. The 8-wave scheme requires the zero divergence to be satisfied to second order accuracy in the initial and boundary condition. Finally the CT and CD schemes require that the initial and boundary conditions are compatible with their particular discretization of $\nabla \cdot \mathbf{B} = 0$ to the accuracy of round off errors.

The projection algorithm is identical with the base scheme if $\nabla \cdot \mathbf{B}^* = 0$ to start with. The transport-flux-CT scheme coincides with the base scheme only for one-dimensional problems with slab symmetry in the other directions. The other CT and CD algorithms modify the result of the base scheme in general. The CT and CD schemes are restricted to structured meshes, the projection scheme works for any grid on which the Poisson equation can be solved (this includes unstructured grids), while the 8-wave form can be used independent of the grid type. The projection step is a global scheme, since it requires the (approximate) solution of a Poisson problem. The other schemes are local, although the CT and the flux-CD algorithms have considerably larger stencil than the base scheme.

The numerical test results are summarized in Table IX for the ten test problems presented in this paper. The relative errors that were shown in the other tables for the individual problems are all normalized to the errors of the most accurate scheme for the given problem. The normalized errors are averaged for the different grid resolutions.

The last row of the table contains a correction factor for each scheme. The correction factors are the cubic root of the cost factors shown in Table I, since in a 2D simulation the grid resolution N_x, N_y and the number of time steps N_t should be decreased by this factor to keep the CPU time the same as if only the base scheme was used. For the majority of the test problems, the convergence rate is approximately first order; thus the error will grow proportional to the correction factor due to the decreased resolution. For second order convergence rate (this only applies to the two Alfvén wave tests) the error should be multiplied with the square of the correction factor. Even for the most expensive projection

TABLE IX
Numerical Errors Relative to the Most Accurate Scheme for Each Test

	Project.	Field-CD	Flux-CT	Flux-CD	8-wave	Tr-flux-CT	Field-CT	Base
Rotated 1D tests								
Alfvén travelling	1.000	2.177	2.491	2.491	1.005	1.290	3.562	1.002
Alfvén standing	1.000	1.374	1.219	1.219	1.599	3.221	1.339	1.168
2D shock $\alpha = 63^\circ$	1.022	1.005	1.000	1.007	1.268	1.014	1.269	1.006
2D shock $\alpha = 45^\circ$	1.000	1.031	1.047	1.047	1.801	1.080	1.298	1.782
2.5D shock tube	1.000	1.137	1.234	1.234	1.023	1.132	1.392	1.333
True 2D tests								
Orszag $t = 1$	1.259	1.000	1.324	1.415	1.425	1.568	1.127	1.498
Orszag $t = 3.14$	1.132	1.000	1.188	1.233	1.411	1.383	1.187	1.893 ^a
Cloud-shock	1.007	1.069	1.000	1.036	1.013	—	1.072 ^b	1.348 ^a
Rotor $p = 1$	1.000	1.220	1.052	1.216	1.023	—	1.530	1.094
Rotor $p = 0.5$	1.000	1.058	1.098	1.116	1.050	1.230 ^a	1.289	1.071
Correction factor	≈ 1.06	1.006	1.018	1.013	1.023	1.022	1.014	1.000

^a Required use of the minmod limiter at some resolution(s).

^b Required averaging of the electric field at some resolution(s).

scheme, the correction factor is only ≈ 1.06 (it depends on the number of iterations, but this is a typical number), while the least expensive field-CD scheme has a correction factor 1.006; thus the corrections will not change the errors dramatically. It is also important to note that these factors are based on CPU timings, which are inherently implementation, compiler, and machine dependent. The correction factors shown in the table are probably upper estimates, since they are calculated for 2D problems using a one-step TVD scheme. For more expensive base schemes, e.g., TVD-MUSCL, the correction factors are smaller. In 3D one should take the fourth root instead of the cubic root when transforming the CPU cost to resolution.

Although a single number cannot fully characterize the quality of a numerical solution, and the tests cannot represent all aspects of numerical MHD simulations, the overall trends are quite clear. Based on the table and the detailed comparison of the solutions, the following points can be made:

- The numerical error is typically dominated by the error close to discontinuities and first order convergence rates are typical for discontinuous solutions.
- The base scheme is less robust than the modified schemes.
- The 8-wave scheme can produce incorrect jump conditions across discontinuities in certain problems.
- The field-CT scheme produces spurious oscillations in many test problems which degrade its accuracy.
- The transport-flux-CT scheme is more complicated, less versatile, and typically not more accurate than the flux-CT scheme.
- The projection, the new field-CD, and the flux-CT schemes are the most accurate for these test problems.

It would be interesting to see how well the different schemes can solve steady state problems, how they can be combined with implicit time integration, or how they can be adapted to hierarchical or adaptively refined meshes; however, these questions are out of the scope of this paper and subject of future research.

APPENDIX A

Momentum Conservation and Lorentz Force

I prove that it is impossible for a *conservative* (which is a necessary property to obtain correct weak solutions) scheme to guarantee that the discretized acceleration due to the Lorentz force is *orthogonal* to the magnetic field in every cell to machine accuracy. The latter property will be called the “orthogonality property” for short. Let’s assume that some “perfect” discretization of the MHD equations is conservative as well as it has the orthogonality property. For sake of simplicity we may assume that this perfect scheme is two dimensional, first order accurate in time, and it advances from time step n to $n + 1$ in a single update. Such a scheme should maintain momentum conservation $\sum (\rho \mathbf{v})_{i,j} = \text{const}$ and orthogonality of \mathbf{B} and the acceleration $\partial(\rho \mathbf{v})/\partial t$ due to the Lorentz force $\mathbf{J} \times \mathbf{B}$ for an arbitrary initial condition that satisfies $\nabla \cdot \mathbf{B} = 0$ in some discrete sense. Therefore it is sufficient to construct a single counter example to show that such a perfect scheme does not exist.

Let the initial condition be $\rho = \text{const}$, $p = \text{const}$, $\mathbf{v} = 0$ everywhere. This ensures that momentum can only change due to the magnetic stresses (cf. Eq. (2)). Let $B^y = 0$ in all cells neighboring cell i, j ; thus the acceleration has to be parallel to the y axis in the neighboring

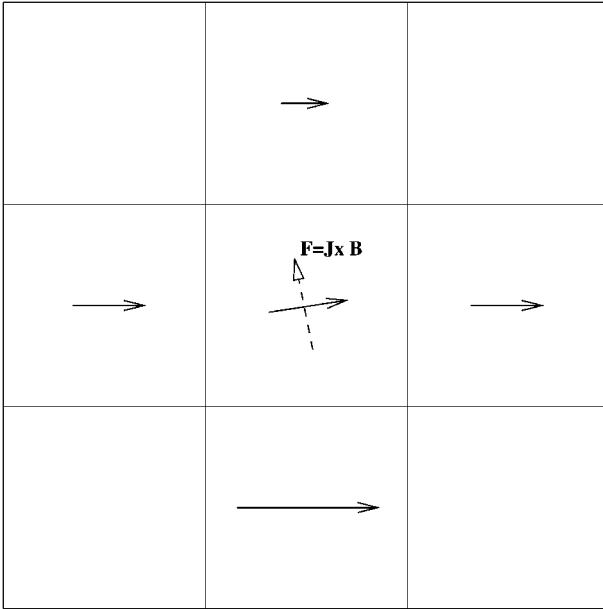


FIG. 21. The discrete magnetic field of the counter example is represented by the solid arrows. The dashed arrow points in the direction of the Lorentz force for the central cell.

cells, which means that ρv^x cannot change in these cells. On the other hand, in cell (i, j) the magnetic field can have a finite B^x component, e.g., $B_{i,j}^x = 1$, and a small non-zero B^y component, e.g., $B_{i,j}^y = \Delta x^k$, which is due to some truncation error. If the current has a finite value, e.g., $J_{i,j}^z = 1$, then the momentum $(\rho v)_{i,j}$ has to change, since the scheme is consistent, and the magnitude of the Lorentz force $|\mathbf{J} \times \mathbf{B}| \approx 1$ is finite. This non-zero momentum change will have to have a non-zero component in the x direction according to the orthogonality property, since $\mathbf{B}_{i,j}$ is not parallel to the x axis. Indeed, the B^x components in the neighboring cells can be chosen such that the current $\mathbf{J}_{i,j} = (\nabla \times \mathbf{B})_{i,j} \neq 0$, for example, $B_{i,j-1}^x = 1.5$, $B_{i-1,j}^x = B_{i+1,j}^x = 1$, and $B_{i,j+1}^x = 0.5$ as it is shown in Fig. 21. It is quite easy to see that the $\nabla \cdot \mathbf{B} = 0$ condition can be satisfied for every cell for a given discretization of $\nabla \cdot \mathbf{B}$, since the number of free parameters, i.e., the components of \mathbf{B} in the surrounding cells, greatly exceeds the number of constraints. In particular, the centered discretization (26) gives $(\nabla \cdot \mathbf{B})_{i,j} = 0$ for the above described initial condition.

As the “perfect scheme” advances the solution with a finite time step, the momentum $(\rho v_x)_{i,j}^{n+1}$ will become non-zero due to the non-zero x component of the acceleration, while in all the neighboring cells $(\rho v_x)^{n+1} = 0$, since there the acceleration due to the Lorentz force has to be exactly orthogonal to the \mathbf{B} field according to the orthogonality property. Consequently, the total ρv_x momentum is not conserved, which means that the “perfect scheme” is not conservative.

APPENDIX B

Generalization of CD/CT Schemes to Curvilinear Grids and Axial Symmetry

Evans and Hawley [14] emphasised that their CT approach is not restricted to Cartesian grids. Here I briefly show how the CT and CD approaches can be combined with

a Godunov-type scheme on arbitrary (non-orthogonal) curvilinear grids. Instead of the general relativistic notation used by Evans and Hawley, I will use the generalized coordinate notation which is more widespread in the computational physics literature.

In this appendix, ξ, η, ζ denote the generalized coordinates, x, y, z the Cartesian coordinates, and any subscripting by these variables indicates a partial derivative, e.g., $x_\xi = \partial x / \partial \xi$. In the generalized coordinate system the grid is uniform, i.e., the j, k, l cell center is located at $j \Delta \xi, k \Delta \eta, l \Delta \zeta$. Let us introduce the curvilinear magnetic and electric field components

$$(\mathcal{B}^\xi, \mathcal{B}^\eta, \mathcal{B}^\zeta)^T = \frac{1}{\det J} J \cdot (B^x, B^y, B^z)^T \quad (\text{B.1})$$

$$(\mathcal{E}^\xi, \mathcal{E}^\eta, \mathcal{E}^\zeta)^T = J^{-1,T} \cdot (E^x, E^y, E^z)^T, \quad (\text{B.2})$$

where the superscripts T indicate the transpose. The Jacobian transformation matrices are

$$J = \begin{pmatrix} \xi_x & \xi_y & \xi_z \\ \eta_x & \eta_y & \eta_z \\ \zeta_x & \zeta_y & \zeta_z \end{pmatrix}, \quad J^{-1,T} = \begin{pmatrix} x_\xi & y_\xi & z_\xi \\ x_\eta & y_\eta & z_\eta \\ x_\zeta & y_\zeta & z_\zeta \end{pmatrix}. \quad (\text{B.3})$$

Note that \mathcal{B} is defined with a $1/\det J$ coefficient in (B.1).

In the curvilinear variables, the induction equation (6) takes the same form as in the Cartesian case! For example, the first component is

$$\frac{\partial \mathcal{B}^\xi}{\partial t} = -\frac{\partial \mathcal{E}^\zeta}{\partial \eta} + \frac{\partial \mathcal{E}^\eta}{\partial \zeta} \quad (\text{B.4})$$

which can be trivially discretized according to the CT or CD approaches, and this guarantees that $\nabla \cdot \mathbf{B} = \partial_\xi \mathcal{B}^\xi + \partial_\eta \mathcal{B}^\eta + \partial_\zeta \mathcal{B}^\zeta$ remains zero in a discrete sense analogous to (15) or (26).

The updated curvilinear components \mathcal{B} can be transformed back to the Cartesian components $\mathbf{B} = \det J J^{-1} \cdot \mathcal{B}$. The elements of the Jacobian matrix can be approximated numerically, e.g., the elements of J^{-1} are

$$(x_\xi)_{j,k,l} = \frac{x_{j+1,k,l} - x_{j-1,k,l}}{2\Delta \xi} \quad (\text{B.5})$$

$$(x_\eta)_{j,k,l} = \frac{x_{j,k+1,l} - x_{j,k-1,l}}{2\Delta \eta},$$

etc., and the elements of J could be obtained by inverting J^{-1} ; however, J is not needed in an efficient implementation.

In two dimensions the equations greatly simplify, since $\mathcal{E}^\xi = \mathcal{E}^\eta = 0$. For slab symmetry in the 3rd direction, the central difference approach (29) becomes

$$B_{j,k}^{x,n+1} = B_{j,k}^{x,n} - \frac{\Delta t}{V_{j,k}} [(x_{j+1,k} - x_{j-1,k})(\mathcal{E}_{j,k+1}^\zeta - \mathcal{E}_{j,k-1}^\zeta) - (x_{j,k+1} - x_{j,k-1})(\mathcal{E}_{j+1,k}^\zeta - \mathcal{E}_{j-1,k}^\zeta)] \quad (\text{B.6})$$

$$B_{j,k}^{y,n+1} = B_{j,k}^{y,n} - \frac{\Delta t}{V_{j,k}} [(y_{j+1,k} - y_{j-1,k})(\mathcal{E}_{j,k+1}^\zeta - \mathcal{E}_{j,k-1}^\zeta) - (y_{j,k+1} - y_{j,k-1})(\mathcal{E}_{j+1,k}^\zeta - \mathcal{E}_{j-1,k}^\zeta)],$$

where $\mathcal{E}^\zeta = E^z = \Omega$ can be approximated by (28) or (31). The (quadrupole) cell volume is defined as

$$V_{j,k} = 4\Delta\xi\Delta\eta \det J^{-1} = (x_{j+1,k} - x_{j-1,k})(y_{j,k+1} - y_{j,k-1}) - (x_{j,k+1} - x_{j,k-1})(y_{j+1,k} - y_{j-1,k}). \quad (\text{B.7})$$

If the magnetic field components are updated according to (B.6) then the following discretization

$$\partial_\xi \mathcal{B}^\xi + \partial_\eta \mathcal{B}^\eta = \frac{\mathcal{B}_{j+1,k}^\xi - \mathcal{B}_{j-1,k}^\xi}{2\Delta\xi} + \frac{\mathcal{B}_{j,k+1}^\eta - \mathcal{B}_{j,k-1}^\eta}{2\Delta\eta} \quad (\text{B.8})$$

is conserved to machine accuracy, where $\mathcal{B}^\xi = y_\eta B^x - x_\eta B^y$, $\mathcal{B}^\eta = -y_\xi B^x + x_\xi B^y$, and the coefficients are defined as in (B.5). To get the usual dimensions for $\nabla \cdot \mathbf{B}$, definition (B.8) can be divided by $V_{j,k}$.

For axial symmetry in the third dimension, $\mathcal{E}^\zeta = z_\zeta E^z = r\Omega$ in (B.6) and the cell volume $V_{j,k}$ (B.7) should also be multiplied by the radial distance r measured from the symmetry axis. If the code is already written in curvilinear vector components, e.g., B^r , B^ϕ on a polar grid, then the only required transformation to obtain \mathcal{B} is a multiplication by $1/\det J$ (which is simply r for polar coordinates).

In an efficient 3D implementation the three curvilinear electric field components $\mathcal{E} = J^{-1.T} \mathbf{E}$ are calculated first. Next the three components of $\partial\mathcal{B}/\partial t$ are obtained according to a CD or CT discretization of (B.4) and its cyclic permutations in ξ, η, ζ . Finally the Cartesian field components are updated

$$\mathbf{B}^{n+1} = \mathbf{B}^n + \Delta t \det J J^{-1} \cdot \partial\mathcal{B}/\partial t, \quad (\text{B.9})$$

where $\det J = 1/\det J^{-1}$ can be calculated and stored in the first time step. Note that the curvilinear magnetic field components \mathcal{B} or the Jacobian J themselves do not occur in this implementation.

ACKNOWLEDGMENTS

The Versatile Advection Code has been developed as part of the project on ‘‘Parallel Computational Magneto Fluid Dynamics,’’ funded by the Dutch Science Foundation (NWO) from 1994 to 1997. The author is currently supported by a postdoctoral fellowship (D 25519) from the Hungarian Science Foundation (OTKA) and by the Bolyai Fellowship from the Hungarian Academy of Sciences. Some high resolution simulations were executed on the Cray T3E in Delft sponsored by the Dutch ‘‘Stichting Nationale Computerfaciliteiten’’ (NCF). Some of the computations were carried out as part of a joint work (in preparation) with Dr. H. C. Yee as a visiting scientist at RIACS, NASA Ames Research Center, August 1998. The joint work concerns the extension of the new Yee *et al.* schemes [49] to MHD.

REFERENCES

1. D. S. Balsara, Linearized formulation of the Riemann problem for adiabatic and isothermal magnetohydrodynamics, *Astrophys. J. Suppl.* **116**, 119 (1998).
2. D. S. Balsara, Total variation diminishing scheme for adiabatic and isothermal magnetohydrodynamics, *Astrophys. J. Suppl.* **116**, 133 (1998).
3. D. S. Balsara and D. S. Spicer, A staggered mesh algorithm using high order Godunov fluxes to ensure solenoidal magnetic fields in magnetohydrodynamic simulations, *J. Comput. Phys.* **149**, 270 (1999).

4. A. A. Barmin, A. G. Kulikovskiy, and N. V. Pogorelov, Shock-capturing approach and nonevolutionary solutions in magnetohydrodynamics, *J. Comput. Phys.* **126**, 77 (1996).
5. J. B. Bell, P. Colella, and H. M. Glaz, A second order projection method for the incompressible Navier–Stokes equations, *J. Comput. Phys.* **85**, 257 (1989).
6. J. P. Boris and D. L. Book, Flux-corrected transport. I. SHASTA, A fluid transport algorithm that works, *J. Comput. Phys.* **11**, 38 (1973).
7. J. U. Brackbill and D. C. Barnes, The effect of nonzero $\nabla \cdot \mathbf{B}$ on the numerical solution of the magnetohydrodynamic equations, *J. Comput. Phys.* **35**, 426 (1980).
8. M. Brio and C. C. Wu, An upwind differencing scheme for the equations of ideal magnetohydrodynamics, *J. Comput. Phys.* **75**, 400 (1988).
9. A. J. Chorin, Numerical solution of the Navier–Stokes equations, *Math. Comp.* **22**, 745 (1968).
10. W. Dai and P. R. Woodward, Extension of the piecewise parabolic method (PPM) to multidimensional magnetohydrodynamics, *J. Comput. Phys.* **111**, 354 (1994).
11. W. Dai and P. R. Woodward, On the divergence-free condition and conservation laws in numerical simulations for supersonic magnetohydrodynamic flows, *Astrophys. J.* **494**, 317 (1998).
12. W. Dai and P. R. Woodward, A simple finite difference scheme for multidimensional magnetohydrodynamic equations, *J. Comput. Phys.* **142**, 331 (1998).
13. C. R. DeVore, Flux-corrected transport techniques for multidimensional compressible magnetohydrodynamics, *J. Comput. Phys.* **92**, 142 (1991).
14. C. R. Evans and J. F. Hawley, Simulation of magnetohydrodynamic flows: A constrained transport method, *Astrophys. J.* **332**, 659 (1988).
15. T. I. Gombosi, K. G. Powell, and D. L. De Zeeuw, Axisymmetric modeling of cometary mass loading on an adaptively refined grid: MHD results, *J. Geophys. Res.* **99**, 21,525 (1994).
16. A. Harten, High resolution schemes for hyperbolic conservation laws, *J. Comput. Phys.* **49**, 357 (1983).
17. M. R. Hestenes and E. Stiefel, Methods of conjugate gradients for solving linear systems, *J. Res. Natl. Bur. Stand.* **49**, 409 (1954).
18. D. E. Innes and G. Tóth, Simulations of small-scale explosive events on the sun, *Solar Phys.* **185**, 127 (1999).
19. R. Keppens and J. P. Goedbloed, Numerical simulations of stellar winds: Polytropic models, *Astron. Astroph.* **343**, 251 (1999).
20. R. Keppens and G. Tóth, Using high performance fortran for magnetohydrodynamic simulations, *Parallel Comput.* **26**(6), 705 (2000).
21. R. Keppens and G. Tóth, Non-linear dynamics of Kelvin–Helmholtz unstable magnetized jets: Three-dimensional effects, *Phys. Plasmas* **6**(5), 1461 (1999).
22. R. Keppens, G. Tóth, R. H. J. Westermann, and J. P. Goedbloed, Growth and saturation of the Kelvin–Helmholtz instability with parallel and anti-parallel magnetic fields, *J. Plasma Phys.* **61**(1), 1 (1999).
23. R. Keppens, G. Tóth, M. A. Botchev, and A. van der Ploeg, Implicit and semi-implicit schemes: Algorithms, *Int. J. Numer. Methods Fluids* **30**, 335 (1999).
24. P. D. Lax and B. Wendroff, Systems of conservation laws, *Comm. Pure Appl. Math.* **13**, 217 (1960).
25. P. Londrillo and L. Del Zanna, High-order upwind schemes for multidimensional magnetohydrodynamics, *Astrophys. J.* **530**, 508 (2000).
26. D. Molteni, G. Tóth, and O. A. Kuznetsov, On the azimuthal stability of shock waves around black holes, *Astrophys. J.* **516**, 411 (1999).
27. D. Odstrčil, Improved FCT algorithm for shock hydrodynamics, *J. Comput. Phys.* **108**, 218 (1993).
28. A. Orszag and C. M. Tang, Small-scale structure of two-dimensional magnetohydrodynamic turbulence, *J. Fluid Mech.* **90**, 129 (1979).
29. R. E. Peterkin, Jr., M. H. Frese, and C. R. Sovinec, Transport of magnetic flux in an arbitrary coordinate ALE code, *J. Comput. Phys.* **140**, 148 (1998).
30. S. Poedts, G. Tóth, J. P. Goedbloed, and A. J. C. Beliën, Nonlinear MHD simulations of wave dissipation in flux tubes, *Solar Phys.* **172**, 45 (1997).

31. K. G. Powell, *An approximate Riemann solver for magnetohydrodynamics* (that works in more than one dimension), ICASE Report No. 94-24, Langley, VA, 1994.
32. D. Ryu, T. W. Jones, and A. Frank, Numerical magnetohydrodynamics in astrophysics: Algorithm and tests for multi-dimensional flow, *Astrophys. J.* **452**, 785 (1995).
33. P. L. Roe, Approximate Riemann solvers, parameter vectors, and difference schemes, *J. Comput. Phys.* **43**, 357 (1981).
34. P. L. Roe and D. S. Balsara, Notes on the eigensystem of magnetohydrodynamics, *SIAM J. Appl. Math.* **56**, 57 (1996).
35. D. Ryu, F. Miniati, T. W. Jones, and A. Frank, A divergence-free upwind code for multi-dimensional magnetohydrodynamic flows, *Astrophys. J.* **509**, 244 (1998).
36. N. A. J. Schutgens and G. Tóth, Numerical simulation of prominence oscillations, *Astron. Astrophys.* **345**, 1038 (1999).
37. H. De Sterck, private communication, 1998.
38. J. M. Stone and M. L. Norman, ZEUS-2D: A radiation magnetohydrodynamics code for astrophysical flows in two space dimensions. II. The magnetohydrodynamic algorithms and tests, *Astrophys. J. Suppl.* **80**, 791 (1992).
39. G. Strang, On the construction and comparison of difference schemes, *SIAM J. Numer. Anal.* **5**, 506 (1968).
40. G. Tóth, A general code for modeling MHD flows on parallel computers: Versatile advection code, *Astrophys. Lett. Comm.* **34**, 245 (1996).
41. G. Tóth, Versatile advection code, in *Lecture Notes in Computer Science* (Springer-Verlag, Berlin, 1997), Vol. 1225, p. 253.
42. G. Tóth, The LASY preprocessor and its application to general multi-dimensional codes, *J. Comput. Phys.* **138**, 981 (1997).
43. G. Tóth, R. Keppens, and M. A. Botchev, Implicit and semi-implicit schemes in the versatile advection code: Numerical tests, *Astron. Astrophys.* **332**, 1159 (1998).
44. G. Tóth and D. Odstrčil, Comparison of some flux corrected transport and total variation diminishing numerical schemes for hydrodynamic and magnetohydrodynamic problems, *J. Comput. Phys.* **128**, 82 (1996).
45. H. A. van der Vorst, Bi-CGSTAB: A fast and smoothly converging variant of Bi-CG for the solution of nonsymmetric linear systems, *SIAM J. Sci. Statist. Comput.* **13**, 631 (1992).
46. B. van Leer, Towards the ultimate conservative difference scheme. V. A second order sequel to Godunov's method, *J. Comput. Phys.* **32**, 101 (1979).
47. M. Vinokur, A rigorous derivation of the MHD equations based only on Faraday's and Ampère's law, presentation at LANL MHD Workshop, 1996.
48. H. C. Yee, A class of high-resolution explicit and implicit shock-capturing methods, NASA TM-101088, 1989.
49. H. C. Yee, N. R. Sandham, and M. J. Djomehri, *High Order Shock-Capturing Methods Using Characteristic Filters*, RIACS Report, May 1998; *J. Comput. Phys.* **150**, 1 (1999).
50. A. L. Zachary, A. Malagoli, and P. Colella, A higher-order Godunov method for multidimensional ideal magnetohydrodynamics, *SIAM J. Sci. Comput.* **15**, 263 (1994).